Turbulent transport of beam ions

T. Dannert,[1,a)] S. Günter,[2] T. Hauff,[2] F. Jenko,[2] X. Lapillonne,[1] and P. Lauber[2]
[1]*Ecole Polytechnique Fédérale de Lausanne (EPFL), Centre de Recherches en Physique des Plasmas, Association Euratom-Confédération Suisse, CH-1015 Lausanne, Switzerland*
[2]*Max-Planck-Institut für Plasmaphysik, Euratom Association, 85748 Garching, Germany*

(Received 21 December 2007; accepted 5 May 2008; published online 25 June 2008)

The radial redistribution of energetic ions by background turbulence is investigated by means of linear and nonlinear gyrokinetic simulations with the GENE code [T. Dannert and F. Jenko, Phys. Plasmas **12**, 072309 (2005)]. The fast particles are described by an asymmetric and anisotropic Maxwellian distribution function, and they are treated as passive tracers. It is found that there can be a significant fast ion diffusivity for particle energies up to about 10 times the thermal energy, with details depending on the properties of the magnetic geometry and of the microinstabilities driving the turbulence. This finding provides a possible explanation of experimental results concerning the efficiency of neutral beam current drive reported recently from ASDEX Upgrade [S. Günter *et al.*, Nucl. Fusion **47**, 920 (2007)]. © *2008 American Institute of Physics*. [DOI: 10.1063/1.2936886]

I. INTRODUCTION

Recent experimental investigations at ASDEX Upgrade (Ref. 1) concerning the efficiency of current drive by neutral beam injection (NBI) showed that the corresponding current profile change decreases above a certain power threshold.[2] Since no relevant magnetohydrodynamic (MHD) activity could be detected, it was conjectured that the background turbulence might lead to anomalous transport of energetic ions across flux surfaces. And indeed, the observed behavior of the current profile could be modelled by introducing a fast ion diffusivity of the order of 0.5 m^2/s in the transport calculations.[2] And as it turns out, it is sufficient if this kind of turbulent redistribution is applied to fast ions with particle energies of up to about 10 times the thermal energy of the plasma.

Earlier transport study experiments at the tokamak fusion test reactor (TFTR) (Ref. 3) found an upper limit of 0.05 m^2/s for the energetic ion diffusion driven by turbulent fluctuations.[4] As in the present paper, this low diffusivity for high parallel velocities was explained by the decorrelation of particles and fields. Later on, in different TFTR experiments the observed fast ion losses could be explained by first orbit loss effects.[5] Furthermore, the fast ion diffusivity could be fully explained by neoclassical effects, and an upper bound for the fast ion diffusivity of 0.1 m^2/s has been found experimentally.[6,7] However, the authors also report some observations where the suggested theory breaks down when the parameters of the experiment are changed. Using a smaller plasma and excluding toroidal field ripple losses, Zweben[8] first described a loss of fast ions which could not be explained by first orbit losses and was not caused by MHD activity. Due to its time delay with respect to the first orbit losses, it was named "delayed loss." It occurred for energies with half of the birth energies of the fusion products. Although these experimental results were obtained for trapped ions, there are similarities to our results presented in this paper. We found a beam ion flux at energies far below the beam energy, which is caused solely by background turbulent fields, which could also serve as an explanation of the mentioned experimental results.

The ASDEX Upgrade studies motivated us to investigate the possible interaction of energetic ions with background turbulence in the framework of gyrokinetic theory and simulation. This interaction could be twofold. First, there might be an influence of the fast ions on the background turbulence, e.g., driving it stronger due to the density gradient of the fast ions, or damping it due to dilution of the driving main ions. Second, the turbulence could influence the fast particle distribution. In particular, in analogy to recent two-dimensional studies,[9] the fast ion curvature drift velocity can be in resonance with the drift velocity of the turbulent eddies (which often resemble the linear properties of the driving microinstabilities, see Refs. 10 and 11). Then the fast particle sees more or less a constant electric field which may lead to strong $E \times B$ drifts, associated with significant cross-field particle transport. In the present paper, we will focus on this second possibility, treating the energetic ions as passive test particles in a turbulent background.

While one finds in the literature a relatively large number of publications on tracer dynamics in which the tracers are assumed to be thermal (see, e.g., Refs. 12–19, and various references therein) or in which (only) finite Larmor radius (FLR) effects are taken into account (see, e.g., Refs. 9, 14, and 20–24, and various references therein), not much is presently known about three-dimensional tracer dynamics with fast parallel motion. In Ref. 25, α particles were modelled as a hot Maxwellian species, such that FLR effects and parallel dynamics effects were mixed. (Moreover, thermal particles were not distinguished from nonthermal ones in this study.) In contrast to that, in the present work, we model a beam ion species by means of an asymmetric and anisotropic Maxwellian distribution function with a long tail in the beam direction, such that it resembles a slowing-down distribution function. Here, FLR effects are clearly subdominant, while drift orbit effects play a central role. An additional passive

a)Electronic mail: Tilman.Dannert@epfl.ch.

particle species with these properties will be used in the gyrokinetic simulations as an idealized model for ions which are injected tangentially via NBI.

The remainder of this paper is organized as follows: In Sec. II, generalized gyrokinetic equations for beam ion species are derived together with the corresponding fluxes and moments. Section III contains the results of linear gyrokinetic simulations along with the construction of a reduced model for the fast ions which captures the key physics of the fast particle dynamics. Section IV deals with nonlinear simulations. Here, we investigate the influence of various turbulence parameters on fast ion diffusion. In Sec. V, we offer a summary of our main results and some conclusions.

II. MODEL EQUATIONS

All simulations presented below are performed with the GENE code[26,10] which solves the nonlinear gyrokinetic equations[27–30] on a fixed grid in five-dimensional phase space, employing the local (flux tube) approximation[31] and a so-called δF splitting. Although GENE can work with realistic magnetohydrodynamic equilibria (see, e.g., Ref. 32), in the present work, an $\hat{s}$-α model geometry[33] is used most of the time for simplicity—the only exception being Sec. III C 2. In order to develop with a reasonably realistic model for beam ions, the standard gyrokinetic equations need to be generalized first. This step is described in the present section.

While the equilibrium distribution function F_0 for thermal electrons and ions is taken to be a Maxwellian (j is the species index, and is e for electrons, i for main ions, and f for beam or fast ions),

$$F_{0j}(v_\parallel,\mu)=\pi^{-3/2}\frac{n_{0j}}{v_{Tj}^3}e^{-(v_\parallel/v_{Tj})^2-\mu B_0/T_{0j}} \tag{1}$$

with the particle density n_{0j}, the temperature T_{0j}, and the thermal velocity

$$v_{Tj}^2=2T_{0j}/m_j, \tag{2}$$

we will describe the fast (beam) ions by an asymmetric and anisotropic Maxwellian distribution function which is given by

$$F_{0f}(v_\parallel,\mu)=\pi^{-3/2}\frac{2n_{0f}}{(v_{T-}+v_{T+})v_{T\perp}^2}e^{-\mu B_0/T_{\perp 0}} \times\{e^{-(v_\parallel/v_{T-})^2}[1-\theta(v_\parallel)]+e^{-(v_\parallel/v_{T+})^2}\theta(v_\parallel)\}. \tag{3}$$

This expression is supposed to be a reasonably realistic but still simple representation of a slowing-down distribution. Here, we have introduced three (potentially) different temperatures: T_{0-} and T_{0+} set the width of the distribution function for negative and positive parallel velocities, respectively, and $T_{\perp 0}$ is the perpendicular temperature of the fast ions. Moreover, $\theta(x)$ denotes the Heaviside step function. For the special case that all of these temperatures are equal to T_{0j}, Eq. (3) turns into Eq. (1). So in what follows, we will rederive the gyrokinetic equations on the basis of Eq. (3). In Fig. 1 the contours of the equilibrium distribution function is shown for typical parameters $T_{0+}=40T_{0f}, T_{0-}=T_{0\perp}=T_{0f}$. In this paper it is assumed that the perpendicular temperature is equal to the background electron temperature. The beam ions are supposed to move along the field lines and therefore the temperature in the negative magnetic field direction is also taken as equal to the background temperature. So the only deviation from the symmetric Maxwellian comes from the larger temperature in field direction which is given by the parameter T_{0+}.

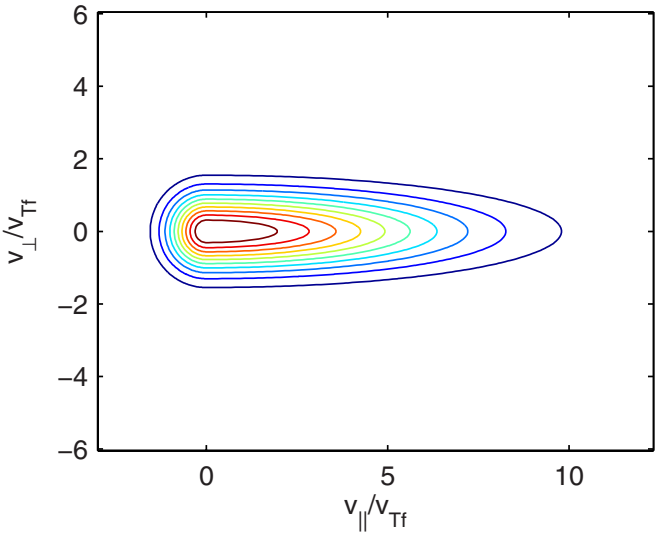

FIG. 1. (Color online) Velocity space contours of the asymmetric Maxwellian distribution function, Eq. (3).

A. Gyrokinetic Vlasov equation

As the starting point for the derivation of the gyrokinetic Vlasov equation employing the equilibrium distribution function F_{0f} from Eq. (3), we use the full-F Vlasov equation which can be found, e.g., in Refs. 28, 29, and 34. It has the form

$$\frac{\partial F}{\partial t}+(v_\parallel\mathbf{b}_0+\mathbf{v}_{E_\chi}+\mathbf{v}_{\nabla B_0}+\mathbf{v}_c)\cdot\left[\nabla F+\frac{1}{mv_\parallel}\left(-e\nabla\bar{\Phi}_1-\frac{e}{c}\dot{\bar{A}}_{\parallel 1}\mathbf{b}_0-\mu\nabla B_0\right)\frac{\partial F}{\partial v_\parallel}\right]=0 \tag{4}$$

with the abbreviations

$$\mathbf{v}_{E_\chi}=\frac{c}{B_0}\mathbf{b}_0\times\nabla\chi_1,\quad \mathbf{v}_{\nabla B_0}=\frac{\mu}{m\Omega}\mathbf{b}_0\times\nabla B_0,$$

$$\mathbf{v}_c=\frac{v_\parallel^2}{\Omega}(\nabla\times\mathbf{b}_0)_\perp$$

for the drift velocities, and the definitions $\Omega=(e_jB_0)/(m_jc)$, $\mathbf{b}_0=\mathbf{B}_0/B_0$, and $\chi_1=\bar{\Phi}_1-(v_\parallel/c)\bar{A}_{\parallel 1}$. Here, the overbars indicate gyroaveraged quantities, $\bar{\Phi}_1=J_0(\lambda_j)\Phi_1$ and

$\bar{A}_{\parallel 1}=J_0(\lambda_j)A_{\parallel 1}$, with $\lambda_j^2=-2\mu B_0/T_{0j}(T_{0j}/T_{0e})(m_j/m_i)(e/e_j)^2\times(B_{\mathrm{ref}}/B_0)^2(\rho_s\nabla_\perp)^2$. We used also $\rho_s=c_s/\Omega_{\mathrm{ref}}$ with $c_s^2=T_{0e}/m_i$ and $\Omega_{\mathrm{ref}}=eB_{\mathrm{ref}}/(m_ic)$.

In the next step, we introduce the δF splitting by writing $F=F_0+F_1$ with $F_1\ll F_0$. We also use the low-β assumption to rewrite the curvature drift as $\mathbf{v}_c=v_\parallel^2/(\Omega B_0)\mathbf{b}_0\times\nabla B_0$ which allows us to combine the ∇B_0 and curvature drift into the drift velocity $\mathbf{v}_d$. If one then introduces the modified distribution function $g=F_1-e/(mc)\partial_{v_\parallel}F_0\bar{A}_{\parallel 1}$, one gets an expression for the general δF Vlasov equation. This equation is then written in terms of vector operators in the following way:

$$\frac{\partial g}{\partial t}+v_\parallel\nabla_\parallel F_1-\frac{e}{m}\frac{\partial F_0}{\partial v_\parallel}\nabla_\parallel\bar{\Phi}_1+\left[\frac{c}{B_0}\mathbf{b}_0\times\nabla\chi+\frac{c}{e_jB_0^2}(\mu B_0+m_jv_\parallel^2)\mathbf{b_0}\times\nabla B_0\right]\cdot\nabla_\perp F_0+\frac{c}{B_0}\mathbf{b}_0\times\nabla\chi\cdot\left(\nabla_\perp F_1-\frac{e}{mc}\frac{\partial F_0}{\partial v_\parallel}\nabla_\perp\bar{A}_{\parallel 1}\right)$$
$$-\frac{\mu}{m}\nabla_\parallel B_0\frac{\partial F_1}{\partial v_\parallel}+\left(\frac{\mu c}{eB_0}+\frac{v_\parallel^2}{\Omega_jB_0}\right)\mathbf{b_0}\times\nabla B_0\cdot\left(\nabla_\perp F_1-\frac{e}{mc}\frac{\partial F_0}{\partial v_\parallel}\nabla_\perp\bar{A}_{\parallel 1}\right)-\frac{e}{mv_\parallel}\frac{\partial F_0}{\partial v_\parallel}\frac{v_\parallel^2}{\Omega_jB_0}\mathbf{b_0}\times\nabla B_0\cdot\nabla_\perp\chi=0.$$

One can identify the parallel dynamics in the second and third term, the drive in the square brackets, the $E\times B$ nonlinearity in the last term of the first line and the mirror term in the first term of the second line. The last two terms are connected to the curvature and ∇B_0 drift.

So we have three kinds of operators which are to be transformed to a field-line following coordinate system with the radial coordinate x, the parallel coordinate z, and the binormal coordinate y, which form a right-handed coordinate system (x,y,z). In a simple $\hat{s}$-α model geometry, the metric coefficients g^{ij} are given by $g^{11}=1$, $g^{12}=g^{21}=\hat{s}z/(q_0R_0)$, $g^{13}=0$, $g^{22}=1+(\hat{s}z/(q_0R_0))^2$, $g^{23}=q_0R_0/r_0$ (see Ref. 31), such that we get the following expressions for the above operators:

$$\mathbf{b}_0\cdot\nabla=\frac{\partial}{\partial z},$$

$$\mathbf{b}_0\times\nabla B_0\cdot\nabla=\frac{\partial B_0}{\partial x}\frac{\partial}{\partial y}-\frac{\hat{s}z}{r_0}\frac{\partial B_0}{\partial z}\frac{\partial}{\partial y}+\frac{q_0R_0}{r_0}\left(\frac{\partial B_0}{\partial x}\frac{\partial}{\partial z}-\frac{\partial B_0}{\partial z}\frac{\partial}{\partial x}\right),$$

$$\mathbf{b}_0\times\nabla\chi\cdot\nabla=\left(\frac{\partial\chi}{\partial x}\frac{\partial}{\partial y}-\frac{\partial\chi}{\partial y}\frac{\partial}{\partial x}\right)+\frac{q_0R_0}{r_0}\frac{\partial\chi}{\partial x}\frac{\partial}{\partial z}+\frac{\hat{s}z}{r_0}\frac{\partial\chi}{\partial y}\frac{\partial}{\partial z},$$

$$\nabla_\perp^2=\frac{\partial^2}{\partial x^2}+2\frac{\hat{s}z}{q_0R_0}\frac{\partial^2}{\partial x\,\partial y}+\left[1+\left(\frac{\hat{s}z}{q_0R_0}\right)^2\right]\frac{\partial^2}{\partial y^2}.$$

All parallel derivatives of perturbed quantities have been neglected due to the assumption $k_\parallel\ll k_\perp$.

Using these expressions together with Eq. (3), and its derivatives (the prime indicates a derivative with respect to the argument)

$$\frac{\partial F_0}{\partial x}=F_0\frac{1}{n_0}\frac{\partial n_0}{\partial x}-F_0\frac{1}{2(v_{T-}+v_{T+})}\left[v_{T-}\frac{T_{0-}'(x)}{T_{0-}}+v_{T+}\frac{T_{0+}'(x)}{T_{0+}}\right]+\frac{mv_\parallel^2}{2}\left[F_{0-}\frac{T_{0-}'(x)}{T_{0-}(x)^2}+F_{0+}\frac{T_{0+}'(x)}{T_{0+}(x)^2}\right]-F_0\frac{T_{\perp 0}'(x)}{T_{\perp 0}(x)}+F_0\frac{\mu B_0}{T_{\perp 0}}\left[\frac{T_{\perp 0}'(x)}{T_{\perp 0}(x)}-\frac{B_0'(x)}{B_0}\right],$$

$$\frac{\partial F_0}{\partial z}=-F_0\frac{\mu B_0}{T_{\perp 0}(x)}\frac{1}{B_0}\frac{\partial B_0}{\partial z},$$

$$\frac{\partial F_0}{\partial v_\parallel}=-F_{0-}\frac{mv_\parallel}{T_{0-}}-F_{0+}\frac{mv_\parallel}{T_{0+}},$$

we arrive at an expression for the Vlasov equation. Introducing the modified distribution function $g=F_1+(ev_\parallel/c)(F_{0-}/T_{0-}+F_{0+}/T_{0+})\bar{A}_{\parallel 1}$, normalizing according to Tables I and II in Ref. 10, using the abbreviations

$$\alpha_j=\frac{v_{Tj}L_\perp}{c_sq_0R_0},\quad \sigma_j=\frac{e_jT_{e0}}{eT_{0j}},$$

$$\tau_{+,-,\perp}=\frac{T_{0+,-,\perp}}{T_{0j}},\quad B_0(x,z)=B_{\mathrm{ref}}\hat{B}(x,z),$$

and the normalized asymmetric equilibrium distribution function

$$F_{0f}=\pi^{-3/2}\frac{2e^{-\mu\hat{B}/\tau_\perp}}{(\sqrt{\tau_-}+\sqrt{\tau_+})\tau_\perp}\times\{e^{-v_\parallel^2/\tau_-}[1-\theta(v_\parallel)]+e^{-v_\parallel^2/\tau_+}\theta(v_\parallel)\},$$

together with the normalized magnetic field $\hat{B}=R_0/[R_0+(r_0+x)\cos z]$ whose derivatives are

$$\frac{\partial\hat{B}}{\partial x}=-\hat{B}^2\frac{L_\perp}{R_0}\cos z,\quad \frac{\partial\hat{B}}{\partial z}=\hat{B}^2\epsilon_t\sin z,$$

we get the final equation

$$\frac{\partial g}{\partial t}+\alpha_j v_\parallel\frac{\partial F_1}{\partial z}+\sigma_j\alpha_j v_\parallel\left(\frac{F_{0-}}{\tau_-}+\frac{F_{0+}}{\tau_+}\right)\frac{\partial\bar{\Phi}_1}{\partial z}-\alpha_j\frac{\mu}{2}\hat{B}^2\epsilon_t\sin z\frac{\partial F_1}{\partial v_\parallel}+\frac{1}{\hat{B}}\left(\frac{\partial\chi}{\partial x}\frac{\partial g}{\partial y}-\frac{\partial\chi}{\partial y}\frac{\partial g}{\partial x}\right)+\mathcal{D}\left(\frac{1}{\hat{B}}\frac{\partial\chi}{\partial y}-\frac{\mu\hat{B}+2v_\parallel^2}{2\sigma_j}\mathcal{K}_x\right)$$
$$+\frac{\mu\hat{B}+2v_\parallel^2}{2\sigma_j}\left(\mathcal{K}_x\frac{\partial g}{\partial x}+\mathcal{K}_y\frac{\partial g}{\partial y}\right)+\left[\frac{F_0\mu\hat{B}}{2\tau_\perp}+v_\parallel^2\left(\frac{F_{0-}}{\tau_-}+\frac{F_{0+}}{\tau_+}\right)\right]\left(\mathcal{K}_x\frac{\partial\chi}{\partial x}+\mathcal{K}_y\frac{\partial\chi}{\partial y}\right)=0 \tag{5}$$

with $\mathcal{K}_x=-2L_\perp/R\sin z$ and $\mathcal{K}_y=-2L_\perp/R_0(\cos z+\hat{s}z\sin z)$. We also used the radial derivative of F_0 in normalized units

$$\frac{\partial F_0}{\partial x}=-\omega_{nj}F_0+\omega_{T-}\left[\frac{\sqrt{\tau_-}F_0}{2(\sqrt{\tau_-}+\sqrt{\tau_+})}-v_\parallel^2\frac{F_{0-}}{\tau_-}\right]$$
$$+\omega_{T+}\left[\frac{\sqrt{\tau_+}F_0}{2(\sqrt{\tau_-}+\sqrt{\tau_+})}-v_\parallel^2\frac{F_{0+}}{\tau_+}\right]$$
$$+\omega_{T\perp}\left(1-\frac{\mu\hat{B}}{\tau_\perp}\right)F_0-F_0\frac{\mu\hat{B}}{\tau_\perp}\frac{1}{B_0}\frac{\partial B_0}{\partial x}$$
$$=-\mathcal{D}-F_0\frac{\mu\hat{B}}{\tau_\perp}\frac{1}{B_0}\frac{\partial B_0}{\partial x},$$

where we introduced the normalized gradients $\omega_{n,T}=L_\perp/L_{n,T}$.

We note in passing that while no collision operators are used in Eq. (5), their effect in creating a slowing-down-type distribution function for the beam ions (represented here by asymmetric Maxwellian) is implicitly taken into account.

B. Moments

1. Moments of the equilibrium distribution function

We first calculate the moments for the equilibrium distribution function, Eq. (3), for further reference.

The density is given by n_{0f} by definition. The parallel velocity $u_{\parallel 0f}$, the first moment in $v_\parallel$ gives

$$u_{\parallel 0f}=\frac{2\pi}{n_{0f}}\frac{B_0}{m_f}\int v_\parallel F_{0f}dv_\parallel d\mu=\frac{v_{T+}-v_{T-}}{\sqrt{\pi}}.$$

It is clear that this moment only exists for an asymmetric F_0. For the pressure, we consider the parallel and the perpendicular pressure independently. For the parallel pressure, we have

$$p_{\parallel 0f}=\frac{m_f}{2}2\pi\frac{B_0}{m_f}\int(v_\parallel-u_{\parallel 0f})^2F_{0f}dv_\parallel d\mu$$
$$=n_{0f}\left[\frac{\pi-2}{2\pi}(T_{0-}+T_{0+})+\frac{4-\pi}{2\pi}\sqrt{T_{0+}T_{0-}}\right]$$

and for the perpendicular pressure

$$p_{\perp 0f}=2\pi\frac{B_0}{m_f}\int\mu B_0F_{0f}dv_\parallel d\mu=n_{0f}T_{\perp 0f}.$$

2. Moments of the perturbed distribution function

For the perturbed distribution function, the calculation is different and subject to this subsection. The moments are defined in particle coordinates as (we use only even moments in $v_\perp$, so $r=2q$)

$$M_{kr}=\int v_\parallel^k v_\perp^{2q}f_1d^3v.$$

Using the pullback operator

$$T^*F=F_{j1}+\frac{e_j}{B_0}\tilde{\Phi}(\mathbf{X}+\mathbf{r})\frac{\partial F_{0j}}{\partial\mu}$$
$$+\frac{e_j}{m_jc}\tilde{A}_{1\parallel}(\mathbf{X}+\mathbf{r})\left(\frac{\partial F_{0j}}{\partial v_\parallel}-\frac{m_jv_\parallel}{B_0}\frac{\partial F_{0j}}{\partial\mu}\right)$$
$$=F_{j1}(\mathbf{X})-\frac{e_j}{T_{\perp 0}}\tilde{\Phi}(\mathbf{X}+\mathbf{r})F_{0j}$$
$$+\frac{e_jv_\parallel}{c}\left(\frac{F_0}{T_{\perp 0}}-\frac{F_{0-}}{T_{0-}}-\frac{F_{0+}}{T_{0+}}\right)\tilde{A}_{1\parallel}(\mathbf{X}+\mathbf{r}),$$

where $\mathbf{X}$ is the position of the gyrocenter and $\mathbf{r}$ is the vector from the gyrocenter to the particle position in the formula for the moments and calculating the integrals explicitly leads to

$$M_{00}=2\pi\frac{B_0}{m_j}\int J_0F_{j1}dv_\parallel d\mu-\frac{e_jn_{0j}}{T_{\perp 0}}(1-\Gamma_0)\left(\Phi_1+\frac{\sqrt{\tau_-}-\sqrt{\tau_+}}{\sqrt{\pi}}\frac{v_{Tj}}{c}A_{1\parallel}\right),$$

$$M_{10}=2\pi\frac{B_0}{m_j}\int v_\parallel J_0F_{j1}dv_\parallel d\mu+\frac{e_jn_{0j}}{T_{\perp 0}}v_{Tj}(1-\Gamma_0)\left[\frac{\sqrt{\tau_-}-\sqrt{\tau_+}}{\sqrt{\pi}}\Phi_1+\frac{1}{2}(\tau_+-\sqrt{\tau_+\tau_-}+\tau_--\tau_\perp)\frac{v_{Tj}}{c}A_{1\parallel}\right],$$

$$M_{20}=2\pi\frac{B_0}{m_j}\int v_\parallel^2J_0F_{j1}dv_\parallel d\mu+\frac{e_jn_{0j}}{T_{\perp 0}}v_{Tj}^2(1-\Gamma_0)\left[-\frac{\tau_+-\sqrt{\tau_+\tau_-}+\tau_-}{2}\Phi_1+\frac{(\sqrt{\tau_+}-\sqrt{\tau_-})(\tau_++\tau_--\tau_\perp)}{\sqrt{\pi}}\frac{v_{Tj}}{c}A_{1\parallel}\right],$$

$$M_{02}=2\pi\frac{2B_0^2}{m_j^2}\int \mu J_0 F_{j1}dv_\parallel d\mu-\frac{v_{Tj}^2 e_j n_{0j}}{T_{0j}}[1-(1-b_j)\Gamma_0-b_j\Gamma_1]\left(\Phi_1-\frac{\sqrt{\tau_+}-\sqrt{\tau_-}}{\sqrt{\pi}}\frac{v_{Tj}}{c}A_{1\parallel}\right),$$

$$M_{12}=2\pi\frac{2B_0^2}{m_j^2}\int v_\parallel \mu J_0 F_{j1}dv_\parallel d\mu+\frac{e_j n_{0j}}{T_{0j}}v_{Tj}^3[1-(1-b_j)\Gamma_0-b_j\Gamma_1]\times\left[\frac{\sqrt{\tau_-}-\sqrt{\tau_+}}{\sqrt{\pi}}\Phi_1+\frac{1}{2}(\tau_+-\sqrt{\tau_+\tau_-}+\tau_--\tau_\perp)\frac{v_{Tj}}{c}A_{1\parallel}\right],$$

$$M_{30}=2\pi\frac{B_0}{m_j}\int v_\parallel^3 J_0 F_{j1}dv_\parallel d\mu+\frac{e_j n_{0j}}{T_{0j}}v_{Tj}^3(1-\Gamma_0)\times\left[-\frac{(\sqrt{\tau_+}-\sqrt{\tau_-})(\tau_++\tau_-)}{\tau_\perp\sqrt{\pi}}\Phi_1+\frac{3}{4}\frac{\tau_+^{5/2}+\tau_-^{5/2}-\tau_\perp(\tau_+^{3/2}+\tau_-^{3/2})}{\tau_\perp(\sqrt{\tau_-}+\sqrt{\tau_+})}\frac{v_{Tj}}{c}A_{1\parallel}\right].$$

Here, we used the function $\Gamma_n(b_j)=\hat{I}_n(b_j)e^{-b_j}$ with the modified Bessel function $\hat{I}_n$. The argument b_j is given by $b_j=-(T_{0j}/T_{e0})(m_j/m_i)(e/e_j)^2(B_{\mathrm{ref}}/B_0)^2(\rho_s\nabla_\perp)^2$. All arguments have been suppressed in the equations above, so that really $J_0=J_0(\lambda_j)$, $\Gamma_0=\Gamma_0(b_j)$, and $\Gamma_1=\Gamma_1(b_j)$. The argument of F_{j1}, of the fields, and of the resulting moments is always the particle coordinate **x**.

Normalizing the moments according to

$$M_{00}=n_{j0}\frac{\rho_s}{L_\perp}\hat{M}_{00},\quad M_{10}=n_{j0}\frac{\rho_s}{L_\perp}c_s\frac{L_\parallel}{L_\perp}\hat{M}_{10},$$

$$M_{20}=n_{j0}\frac{\rho_s}{L_\perp}v_{Tj}^2\hat{M}_{20},\quad M_{02}=n_{j0}\frac{\rho_s}{L_\perp}v_{Tj}^2\hat{M}_{02},$$

$$M_{12}=n_{j0}\frac{\rho_s}{L_\perp}v_{Tj}^2c_s\frac{L_\parallel}{L_\perp}\hat{M}_{12},\quad M_{30}=n_{j0}\frac{\rho_s}{L_\perp}v_{Tj}^2c_s\frac{L_\parallel}{L_\perp}\hat{M}_{30},$$

one can easily express them with respect to our usual units. With their help, we will construct the physical moments and the transport fluxes in Sec. II D. For diagnostic purposes, we also introduce the integrals over the parallel velocity coordinate. To simplify the notation we use the μ-integrated equilibrium distribution function $F_{0j}(v_\parallel)$ which is given by

$$\begin{aligned}F_{0j}(v_\parallel)&=2\pi\frac{B_0}{m_j}\int_0^\infty F_{0j}(v_\parallel,\mu)d\mu\\&=\frac{1}{\sqrt{\pi}}\frac{2n_{0j}}{v_{T-}+v_{T+}}\{e^{-(v_\parallel/v_{T-})^2}[1-\theta(v_\parallel)]\\&\quad+e^{-(v_\parallel/v_{T+})^2}\theta(v_\parallel)\}.\end{aligned}\tag{6}$$

C. Gyrokinetic field equations

Although in the present paper, we treat the fast particles only as passive tracers, i.e., we do not model the back reaction of these particles on the fields, we still derive the self-consistent field equations here for future reference. The quasineutrality condition and Ampere's law read

$$\sum_j e_j n_j=0,\quad -\nabla_\perp^2 A_{\parallel 1}=\frac{4\pi}{c}j_{\parallel 1}.$$

Expressing the perturbed parallel current density in units of $en_{e0}c_sL_\parallel/L_\perp\rho_s/L_\perp$, and the perturbed density in units of $n_{0j}\rho_s/L_\perp$, we can write the normalized field equations as

$$\sum_j \xi_j n_{1j}=0,\quad -\nabla_\perp^2 A_{\parallel 1}=\sum_j \xi_j j_{\parallel 1j}$$

with $\xi_j=e_jn_{0j}/(en_{e0})$.

The perturbed particle and current density are given, respectively, by the moments M_{00} and M_{10} as defined above. If we also use the modified distribution function g which in normalized units reads

$$g=F_1+\sigma_j\alpha_j v_\parallel\hat{\beta}\left(\frac{F_{0-}}{\tau_-}+\frac{F_{0+}}{\tau_+}\right)\bar{A}_{\parallel 1},$$

we arrive at the final system of field equations,

$$\sum_j P_j^{(1)}\Phi_1(\mathbf{x})+\sum_j Q_j^{(1)}A_{\parallel 1}(\mathbf{x})=\sum_j \xi_j\pi\hat{B}\int J_0(\lambda_j)g dv_\parallel d\mu,\tag{7}$$

$$\sum_j P_j^{(2)}\Phi_1(\mathbf{x})+\left[-\nabla_\perp^2+\sum_j Q_j^{(2)}\right]A_{\parallel 1}(\mathbf{x})=\sum_j \xi_j\alpha_j\pi\hat{B}\int v_\parallel J_0(\lambda_j)g dv_\parallel d\mu.\tag{8}$$

The prefactors are

$$P_j^{(1)}=\xi_j\frac{\sigma_j}{\tau_\perp}[1-\Gamma_0(b_j)],$$

$$Q_j^{(1)}=\xi_j\sigma_j\alpha_j\hat{\beta}\left\{\frac{\sqrt{\tau_-}-\sqrt{\tau_+}}{\tau_\perp\sqrt{\pi}}[1-\Gamma_0(b_j)]+\Upsilon_j\right\},$$

$$P_j^{(2)}=-\xi_j\sigma_j\alpha_j\frac{\sqrt{\tau_-}-\sqrt{\tau_+}}{\tau_\perp\sqrt{\pi}}[1-\Gamma_0(b_j)],$$

$$Q_j^{(2)}=-\hat{\beta}\xi_j\frac{\sigma_j\alpha_j^2}{2}\frac{\tau_+-\sqrt{\tau_+\tau_-}+\tau_--\tau_\perp}{\tau_\perp}[1-\Gamma_0(b_j)]+\hat{\beta}\xi_j\alpha_j^2\sigma_j Y_j.$$

In this context, we would like to point out that the two field equations are only coupled if one uses an asymmetric Maxwellian. For $\tau_+=\tau_-$, the coupling terms $Q_j^{(1)}$ and $P_j^{(2)}$ vanish, and the electrostatic potential is solely determined by the density while the parallel electromagnetic potential is given

by the parallel current density alone. Due to the usage of the modified distribution function, the two operators

$$\Upsilon_j = \pi\hat{B}\int v_\parallel\left(\frac{F_{0-}}{\tau_-}+\frac{F_{0+}}{\tau_+}\right)J_0(\lambda_j)^2 dv_\parallel d\mu,$$

$$Y_j = \pi\hat{B}\int v_\parallel^2\left(\frac{F_{0-}}{\tau_-}+\frac{F_{0+}}{\tau_+}\right)J_0(\lambda_j)^2 dv_\parallel d\mu$$

have been introduced. These functions could be evaluated analytically and would then give $\Upsilon_j=0$ and $Y_j=\Gamma_0(b_j)/2$. To avoid numerical integration errors of the $A_\parallel$ part of the modified distribution function, which occur on the right-hand side integrals in the system of equations, we also calculate the two functions Υ_j and Y_j numerically with the same method as the right-hand side integrals.

For the solution of Eqs. (7) and (8), one can transform to Fourier space in both perpendicular directions. This turns all differential operators $\Gamma_0(b_j)$, $J_0(\lambda_j)$, Υ_j, Y_j into algebraic ones. In what follows in Secs. III and IV, we use the two equations for the background only, where they decouple by using the following expression for the prefactors:

$$P_j^{(1)} = \xi_j\sigma_j[1-\Gamma_0(b_j)],$$

$$Q_j^{(1)} = P_j^{(2)} = 0,$$

$$Q_j^{(2)} = \hat{\beta}\xi_j\alpha_j^2\sigma_j Y_j.$$

Additionally the species index j only runs over the background species, i.e., the electrons and the main ions.

In principle, it is also necessary to use a third field equation for the perturbation of the parallel magnetic field $B_\parallel$. However, it is well known that this field variation is proportional to the β value (β is the ratio between plasma pressure and magnetic pressure). In all of our simulations we used a $\beta_e=4\pi n_{0e}T_{0e}/B_{\mathrm{ref}}^2$ of 0.1%, so for electrons and main ions the $B_\parallel$ fluctuations are negligible. For the beam ions we have a parallel $\beta_{\parallel f}$ of

$$\beta_{\parallel f} = \frac{n_{0f}}{n_{0e}}\frac{T_{0f}}{T_{0e}}\left[\frac{\pi-2}{2\pi}(\tau_-+\tau_+)+\frac{4-\pi}{2\pi}\sqrt{\tau_+\tau_-}\right]\beta_e.$$

So, if we take $T_{0f}=T_{0e}$ (T_{0f} is only a normalization temperature for the beam ions) and use common densities of the beam ions of $n_{0f}/n_{0e}<10\%$, we get a $\beta_{\parallel f}$ for our standard parameters (cf. Sec. III) of $\beta_{\parallel f}\approx 0.8\beta_e$. This value is even lower as for the main ions and electrons and therefore the $B_\parallel$ fluctuations can be safely neglected.

D. Transport fluxes and physical moments

Our main interest concerns the transport of fast particles. To this end we have to calculate transport fluxes and diffusivities together with the physical moments from the distribution function and the potentials.

1. Particle flux

Starting with the radial particle flux, which is defined in particle coordinates as

$$\Gamma(\mathbf{x}) = \int v_x(\mathbf{x})f_1(\mathbf{x})d^3v,$$

and using the generalized $E\times B$ velocity,

$$v_x = -\frac{c}{B_0}\frac{\partial\chi}{\partial y} = -\frac{c}{B_0}\left(\frac{\partial\Phi}{\partial y}-\frac{v_\parallel}{c}\frac{\partial A_{1\parallel}}{\partial y}\right) = v_{E,x}+v_\parallel\frac{B_{1,x}}{B_0},$$

which consists of an electrostatic contribution due to the standard $E\times B$ drift and an electromagnetic contribution from the motion along the perturbed field lines, one arrives at

$$\Gamma = v_{E,x}\int f_1 d^3v + \frac{B_{1,x}}{B_0}\int v_\parallel f_1 d^3v$$

$$= v_{E,x}M_{00}+\frac{B_{1,x}}{B_0}M_{10} = \Gamma_{\mathrm{es}}+\Gamma_{\mathrm{em}},$$

where we used the formerly calculated moments and divided the flux in an electrostatic and an electromagnetic contribution. Normalization leads to

$$\hat{\Gamma}_{\mathrm{es}} = \hat{v}_{E,x}\hat{M}_{00}, \quad \hat{\Gamma}_{\mathrm{em}} = \hat{B}_{1,x}\hat{M}_{10}$$

with $\hat{v}_{E,x}=-\hat{B}^{-1}(\partial\Phi_1/\partial y)$ and $\hat{B}_{1,x}=\hat{B}^{-1}\hat{\beta}(\partial A_{\parallel 1}/\partial y)$. The particle fluxes then have units of $D_{\mathrm{GB}}\ (n_{0j}/L_\perp)$ with the gyro-Bohm diffusivity related to the macroscopic length scale $L_\perp$ given as $D_{\mathrm{GB}}=c_s\rho_s(\rho_s/L_\perp)$.

2. Flux of the parallel momentum

The parallel momentum flux is defined as

$$\Pi_\parallel(\mathbf{x}) = \int mv_\parallel v_x(\mathbf{x})f_1(\mathbf{x})d^3v.$$

From this definition we obtain

$$\Pi_\parallel = m\int v_{E,x}v_\parallel f_1 d^3v + m\int v_\parallel^2 f_1\frac{B_{1,x}}{B_0}d^3v$$

$$= mv_{E,x}M_{10}+m\frac{B_{1,x}}{B_0}M_{20},$$

and with the usual normalization [the flux itself is normalized according to $\Pi_\parallel=n_{0j}D_{\mathrm{GB}}(L_\parallel/L_\perp)(m_jc_s/L_\perp)\hat{\Pi}_\parallel$, we get

$$\hat{\Pi}_\parallel = \hat{v}_{E,x}\hat{M}_{10}+\alpha_j^2\hat{\beta}\hat{B}_{1,x}\hat{M}_{20}.$$

3. Heat flux

The heat flux is defined as the flux of kinetic energy in radial direction,

$$Q(\mathbf{x}) = \int\frac{mv^2}{2}v_x(\mathbf{x})f_1(\mathbf{x})d^3v.$$

This leads to the expression

$$Q = \frac{m}{2} v_{E,x}(M_{20} + M_{02}) + \frac{m}{2}\frac{B_{1,x}}{B_0}(M_{30} + M_{12}) = Q_{\mathrm{es}} + Q_{\mathrm{em}},$$

which in normalized units reads

$$\hat{Q} = \hat{v}_{E,x}(\hat{M}_{20} + \hat{M}_{02}) + \hat{B}_{1,x}(\hat{M}_{30} + \hat{M}_{12}).$$

Here, the heat flux units are $D_{\mathrm{GB}}(n_{0j}T_{0j}/L_{\perp})$.

4. Physical moments

The zeroth physical moment is clearly the particle density n_{1j} which is already calculated as the moment M_{00}. The next moment in the hierarchy is the parallel velocity

$$u_{\parallel 1j} = \frac{1}{n_{0j}} M_{10},$$

which in normalized units reads $\hat{u}_{\parallel 1j} = \hat{M}_{10}$.

One gets the moment of the parallel temperature from the following definition:

$$\frac{1}{2} n T_{\parallel} = p_{\parallel} = \frac{m}{2} \int (v_{\parallel} - u_{\parallel})^2 f d^3 v.$$

To first order in the perturbations, we thus arrive at the expression

$$T_{\parallel 1j} = \frac{T_{0j}}{n_{0j}} \left\{ \left[\frac{4}{\pi} (\sqrt{\tau_+} - \sqrt{\tau_-})^2 - (\tau_- - \sqrt{\tau_+ \tau_-} + \tau_-) \right] M_{00} - \frac{4}{v_{Tj}} \frac{\sqrt{\tau_+} - \sqrt{\tau_-}}{\sqrt{\pi}} M_{10} + \frac{2}{v_{Tj}^2} M_{20} \right\}$$

for the parallel temperature perturbation. In normalized units, we get

$$\hat{T}_{\parallel 1j} = 2\hat{M}_{20} - \frac{4}{\alpha_j} \frac{\sqrt{\tau_+} - \sqrt{\tau_-}}{\sqrt{\pi}} \hat{M}_{10} + \left[\frac{4}{\pi} (\sqrt{\tau_+} - \sqrt{\tau_-})^2 - \tau_- + \sqrt{\tau_+ \tau_-} - \tau_- \right] \hat{M}_{00}. \tag{9}$$

Finally, using

$$n T_{\perp} = \frac{m}{2} \int v_{\perp}^2 f d^3 v$$

and the same procedure as for the parallel temperature, we arrive at the expression

$$T_{\perp 1j} = \frac{m_j}{2 n_{0j}} M_{02} - T_{\perp 0} \frac{M_{00}}{n_{0j}}$$

for the perpendicular temperature which in normalized units reads

$$\hat{T}_{\perp 1j} = \hat{M}_{02} - \tau_{\perp} \hat{M}_{00}. \tag{10}$$

E. Numerical issues

In the following two sections, we will report on linear and nonlinear gyrokinetic simulations with GENE, using the equations derived above. In this context, the numerical treatment of the asymmetric Maxwellian distribution function poses several problems. The maximum parallel velocity which has to be taken into account in the simulation is now higher than for a symmetric Maxwellian where it is usually around $3v_{Tj}$. But on the other hand, the higher the maximal velocity is, the more computationally expensive are the simulations. As a compromise, we will set the upper $v_{\parallel}$ boundary to 65% of $3v_{T+}$. This "rule" yields, e.g., an upper boundary of 12.33 for $\tau_+ = 40$. To keep the $v_{\parallel}$ resolution on the positive side comparable to the one of the negative side, we have to use more grid points for the positive velocities. So the asymmetry is reflected also in the velocity space grid. This leads to a different number of grid points for different species which in turn leads to a severe load unbalancing, as we naturally parallelize over the species. To overcome these problems, an inhomogeneous parallelization has been applied to the GENE code which re-establishes load balancing.

III. LINEAR SIMULATIONS

While nonlinear simulation results will be shown and discussed in Sec. IV, in the following, we will first present results from linear gyrokinetic simulations in order to get some basic insights into the effect of background turbulence on energetic ions. In particular, we will construct a quasilinear model which will allow us to explain the behavior of the fast particle fluxes on a semiquantitative level.

In these GENE simulations, three particle species are kept: electrons and main ions—which drive the microinstabilities and thus the background turbulence—as well as a third passive species representing the fast ions. As standard parameters for the main ions and the electrons we use a dataset inspired by ASDEX Upgrade experiments, namely, $R/L_n = 3$, $R/L_{Te} = 8$, $R/L_{Ti} = 9$, $\beta_e = 4\pi n_{0e} T_{0e} B_{\mathrm{ref}}^{-2} = 0.1\%$, $q = 1.4$, $\hat{s} = 0.8$, $\epsilon_t = r/R = 0$, and $T_{0e} = T_{0i}$. For the mass ratio we use $m_i/m_e = 400$ since this helps to save computational time while the relevant properties (mainly the complex frequencies) of the underlying microinstabilities do not change much when going to realistic values.

For these parameters, the turbulence is driven by toroidal ion temperature gradient (ITG) modes. In Fig. 2, the k_y spectra of the real frequencies and linear growth rates are shown for the standard parameter set. Here, we use the convention that a negative real frequency represents a drift in the ion diamagnetic direction while a positive frequency indicates a drift in the electron diamagnetic direction. In the k_y range between about $k_y \rho_s = 0.1$ and $k_y \rho_s = 0.5$, we find toroidal ITG modes. At much higher wavenumbers, electron temperature gradient (ETG) modes are also unstable, but they will be neglected in the following, as we are interested only in ion scales.

For the beam ions we use a strong density gradient of $R/L_{nf} = 15$ and assuming a beam directed tangentially along the field line, $\tau_{\perp} = \tau_- = 1$, $\tau_+ = 40$.

A. A quasilinear model

To identify the physical mechanisms determining the interaction of fast ions with given fields, we try to reduce the model used for the fast ions to the least complicated version which still retains all relevant features. To this end, we

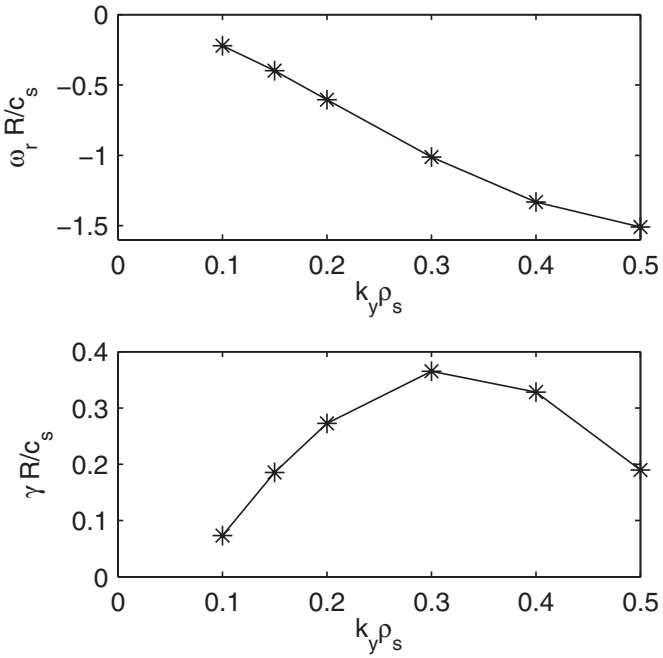

FIG. 2. Real frequencies ω_r and linear growth rates γ for the standard parameters mentioned in the text, describing toroidal ion temperature gradient (ITG) modes.

switch off different terms in the fast ion Vlasov equation and investigate the changes in parallel velocity space. The equations of the background ions and electrons are left untouched. The full model yields the results shown in Fig. 3. This figure reveals that most of the transport is carried by

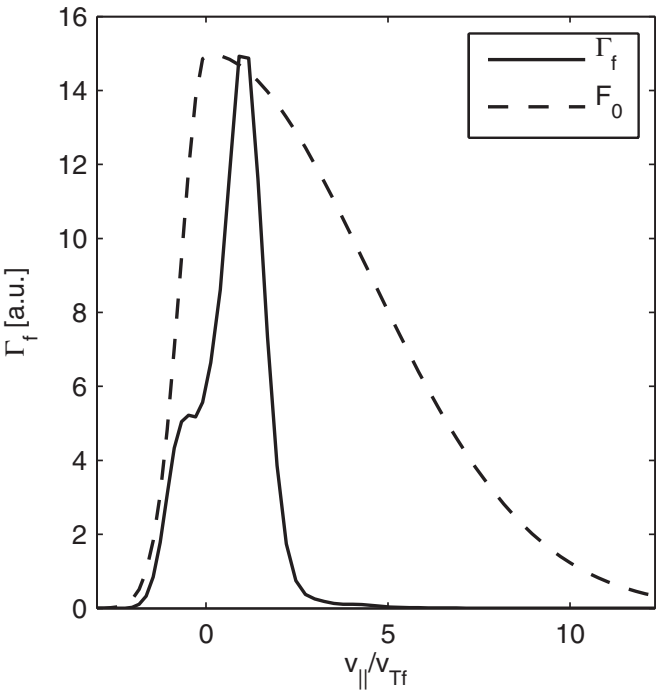

FIG. 3. Fast particle flux Γ_f (solid line) as a function of the parallel velocity $v_\parallel$ for $\tau_+=40$, averaged over k_y. Also the equilibrium distribution function, Eq. (6), is shown. The left and right thermal velocities are at $v_{T-}/v_{Tf}=-1$ and $v_{T+}/v_{Tf}=\sqrt{40}$.

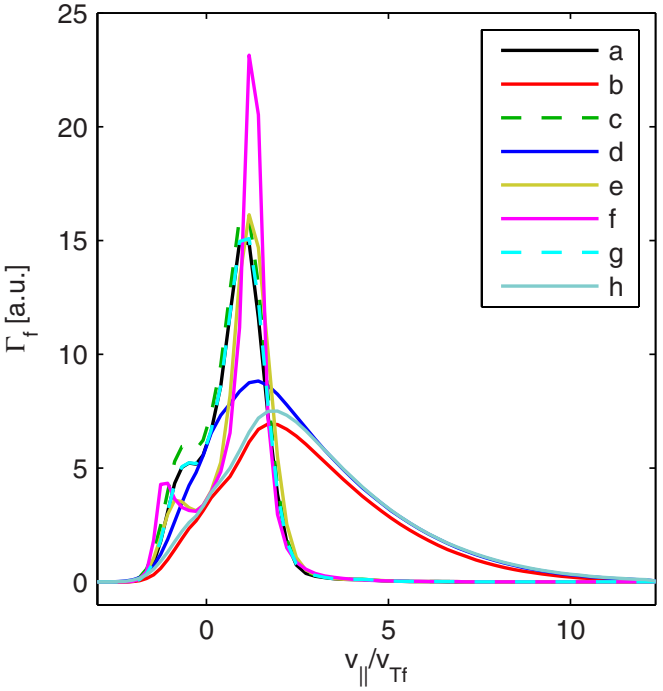

FIG. 4. (Color online) Fast particle flux Γ_f as a function of parallel velocity $v_\parallel$ for different reduced models. Shown are the full Vlasov equation (a), Eq. (11) (b), Eq. (12) (c), $\mathcal{K}_x=0$ and only the ∇B drift terms (d), $\mathcal{K}_x=0$ and only the curvature drift terms (e), Eq. (13) (f), $\mathcal{K}_x=0$ (g) and $\mathcal{K}_y=0$ (h).

almost-thermal particles, while the high-velocity contributions are suppressed. This type of behavior should be captured by any reduced model.

In the first step, we switch off the radial or binormal components of the curvature and ∇B drifts by setting $\mathcal{K}_x=0$ or $\mathcal{K}_y=0$. The results are shown, respectively, as the lines labelled (g) and (h) in Fig. 4, exhibiting that the y components are crucial for the suppression of the particle flux for higher parallel velocities while the x components are not. Here, the thick black curve [label (a)] is the full model which serves as a reference. Models which are further reduced are also shown in Fig. 4. The line labelled (b) indicates the result obtained by using the equation

$$\frac{\partial g}{\partial t} + \alpha_j v_\parallel \frac{\partial F_1}{\partial z} + \sigma_j \alpha_j v_\parallel \left(\frac{F_{0-}}{\tau_-} + \frac{F_{0+}}{\tau_+} \right) \frac{\partial \bar{\Phi}_1}{\partial z} + \omega_{n_j} F_0 \left(\frac{1}{\hat{B}} \frac{\partial \chi}{\partial y} \right) + \left[\frac{F_0 \mu \hat{B}}{2\tau_\perp} + v_\parallel^2 \left(\frac{F_{0-}}{\tau_-} + \frac{F_{0+}}{\tau_+} \right) \right] \times \left(\mathcal{K}_y \frac{\partial \chi}{\partial y} \right) = 0 \tag{11}$$

which neglects the effect of $\mathcal{K}_y$ on the distribution function, but not on the fields. In contrast, the curve (c) in Fig. 4 neglects the effect of $\mathcal{K}_y$ on the fields, but not on the distribution function as described by the equation

$$\frac{\partial g}{\partial t} + \alpha_j v_\parallel \frac{\partial F_1}{\partial z} + \sigma_j \alpha_j v_\parallel \left(\frac{F_{0-}}{\tau_-} + \frac{F_{0+}}{\tau_+} \right) \frac{\partial \bar{\Phi}_1}{\partial z} + \omega_{n_j} F_0 \left(\frac{1}{\hat{B}} \frac{\partial \chi}{\partial y} \right) + \frac{\mu \hat{B} + 2v_\parallel^2}{2\sigma_j} \left(\mathcal{K}_y \frac{\partial g}{\partial y} \right) = 0. \tag{12}$$

One can see that it is necessary to include the drift of the distribution function, whereas the field contribution can be neglected. It will be shown later that the field contribution turns out to be the origin of a small inward flux, however.

Next, the lines (d) and (e) are compared. The line (d) results only include the ∇B drift, the line (e) results only the curvature drift. Since the fast particles are modelled with an anisotropic Maxwellian, we expect the curvature drift to dominate the ∇B drift. This is also what the comparison of the two lines shows.

To complete the reduction, we also switch off the parallel dynamics, which leads to the line with label (f). Here, the change of the shape of the particle transport is larger, but it stays qualitatively the same, i.e., the high velocities still do not contribute to the particle transport. Hence, for the simplest model, one may neglect the parallel dynamics. We note in passing that the Alfvén velocity for our standard parameters is given by $v_A \approx 22 v_{Tf}$, such that the interaction of fast particles with Alfvén waves can safely be neglected. This might change, in principle, for higher β values, where the Alfvén resonance will occur already at lower parallel velocities.

According to this reduction process, it turns out that one can model the fast ions by the very simple Vlasov equation

$$\frac{\partial F_1}{\partial t} + \omega_{n_j} F_0 \frac{1}{\hat{B}} \frac{\partial \bar{\Phi}_1}{\partial y} + \frac{1}{\sigma_j} v_\parallel^2 \mathcal{K}_y \frac{\partial F_1}{\partial y} = 0, \tag{13}$$

which is depicted as the line with label (f) in Fig. 4. This equation still depends on the parallel coordinate via the $\mathcal{K}_y$ term, but all parallel positions are independent, so z is only a parameter in the equation. Equation (13) describes a set of particles which drift in the y direction (representing the toroidal direction in our field-aligned coordinate system) according to the curvature, and which are, at the same time, advected radially by the background potential. Here, we would like to emphasize the fact that all simulations in this paper are done with the *full* Vlasov equation; the reduced model only serves to gain a better understanding of the dynamics.

At this point, one can already make an important observation. From a physical point of view, one may expect the fast particle transport to be large when their curvature drift velocity matches the diamagnetic drift velocity of the background microinstabilities (or turbulence). A similar kind of resonance phenomenon has been observed in Ref. 9, and it is likely that this effect carries over to the present situation. Now, the curvature drift frequency of the fast ions in Eq. (13) is given by

$$\omega_{c,y} = k_y \frac{1}{\sigma_j} v_\parallel^2 \left[-\frac{2L_\perp}{R_0} (\cos z + \hat{s} z \sin z) \right]. \tag{14}$$

Thus, for large parallel velocities, $\omega_{c,y}$ goes up to very high values which are way above the mode frequency imposed from the main ions and electrons. The mode frequencies are in the range of unity in our normalized units, so we can find a frequency match between the fast ion curvature drift frequency and the mode frequency at parallel velocities around $1 v_{Tj}$ to $3 v_{Tj}$, if using, for example, $k_y = 0.1 - 0.3$, $L_\perp / R = 1$, and $z = 0$. This is exactly where we find the main contributions to the particle transport.

If in Eq. (13), one writes F_1 as a superposition of plane waves, $F_1(x,y,z) = \Sigma_m F_m(x,z) e^{-i\omega t + i k_m y}$ with frequency $\omega = \omega_r + i\gamma$, one arrives at the following equation for the perturbed distribution function of the fast ions if one imposes an external electrostatic potential $\bar{\Phi} = \Sigma_m \Phi_m e^{-i\omega t + i k_m y}$,

$$F_m = \frac{k_m \omega_{n_j} F_0}{\hat{B} \left(\omega_r - \frac{v_\parallel^2 \mathcal{K}_y k_m}{\sigma_j} + i\gamma \right)} \Phi_m. \tag{15}$$

This relation can be used to calculate the phase relation between the distribution function and the electrostatic potential. One obtains the expression

$$\tan \varphi_F = \frac{\omega' \tan \varphi_\Phi - \gamma}{\omega' + \gamma \tan \varphi_\Phi}$$

with the Doppler shifted frequency $\omega' = \omega_r [1 - (v_\parallel^2 \mathcal{K}_y / \sigma_j)(k_m / \omega_r)] = \omega_r (1 - v_{c,y} / v_{\text{phase}})$ and the phase angles φ_F of F_m and φ_Φ of Φ. From this relation it can be clearly seen that the phase angle of F_m approaches the phase angle of Φ if the velocity increases.

The second effect which controls the transport of the fast ions has already been mentioned briefly above. The curvature drift of the fast ions in a drifting background potential can be described by defining an effective drift velocity in terms of the difference of the corresponding individual velocities. As has been shown in Ref. 9, the tracer transport falls off quite rapidly as the effective drift velocity becomes finite. In other words, one gets a resonance if the two drift velocities are similar. As will be shown below, the height of this resonance peak of the fast particle diffusivity can be comparable to the turbulent diffusivities of the (thermal) main ions in the plasma.

Hence, for high energy particles, there are two effects which control their transport. One is that the Doppler shifted frequency (which is the mode frequency seen by the curvature drifting fast ion) becomes large and therefore gets out of resonance with the diamagnetic or mode frequency. The other effect is that the phase difference between moments (calculated from the distribution function) and the electrostatic potential decreases. So we expect a phase relation which is smeared over a range of angles, and which is centered around a phase difference of zero. Both effects apply to particle, heat, and momentum fluxes.

From Eq. (15), one can also directly calculate the particle flux via the integral (neglecting $A_\parallel$ contributions and FLR effects)

$$\Gamma_m = \Re\left[\frac{ik_m\Phi_m^*}{\hat{B}}\cdot\hat{M}_{00,m}\right]$$
$$= \frac{2k_m^2\omega_{n_j}\pi^{-1/2}}{(\sqrt{\tau_-}+\sqrt{\tau_+})}\frac{1}{\hat{B}^2}|\Phi_m|^2$$
$$\times\gamma\int\frac{\{e^{-v_\parallel^2/\tau_-}[1-\theta(v_\parallel)]+e^{-v_\parallel^2/\tau_+}\theta(v_\parallel)\}}{\omega'^2+\gamma^2}dv_\parallel.$$

Or, if "undoing" the parallel velocity integration, we come to an expression of the particle flux Γ as a function of $v_\parallel$. Using Eq. (6), we can write for the particle flux,

$$\Gamma_m(x,z,v_\parallel,t) = k_m^2\omega_{n_j}\frac{\gamma}{\hat{B}^2}|\Phi_m(x,z,t)|^2\frac{F_{0j}(v_\parallel)}{\omega'^2+\gamma^2}. \quad (16)$$

What one can see clearly from this expression is that the only dependence of the flux on $\tau_\pm$ comes through the equilibrium distribution function $F_{0j}(v_\parallel)$. We now look at the quantity $\Gamma_m(v_\parallel)/[F_{0j}(v_\parallel)\omega_{nj}]$, which has the meaning of a $v_\parallel$-local diffusivity $D(v_\parallel)$ and obtain a $\tau_\pm$ independent curve. That this really reflects the full model is shown in Sec. III B 1. In physical terms, this finding means that the velocity range for which the fast ions are redistributed by the background microinstabilities is independent of the beam energy. Instead, it is set by the thermal energy of the background plasma.

One can also deduce another very important property of the fast particle diffusivity: Its peak value is expected to be comparable to the diffusivities characterizing the turbulent background. This can be seen as follows. In the model for $D(v_\parallel)$, the $v_\parallel$ dependence only comes into play through the Doppler shifted frequency ω',

$$D(k_m,z,v_\parallel) = \frac{\gamma}{\omega'^2+\gamma^2}\frac{k_m^2|\Phi_m(x,z)|^2}{\hat{B}^2}$$
$$= \frac{\gamma^2}{\omega'^2+\gamma^2}D_{\mathrm{turb}}(k_m,z) \le D_{\mathrm{turb}}(k_m,z). \quad (17)$$

Here, we have introduced the well-known weak turbulence expression for the turbulent diffusivity, $D_{\mathrm{turb}}=v_E^2/\gamma$ (see, e.g., Ref. 12). The maximum of $D(v_\parallel)$ will occur where ω' becomes minimal, and this is the case where either $\omega'=0$ or $\partial\omega'/\partial v_\parallel=0$. As some algebra shows, the second possibility leads to a condition for the parallel position which is independent of the parallel velocity. So to determine the position of the maximum of the diffusivity in $v_\parallel$ space, we must find the roots of ω'. These are at $v_{\parallel,0}=\pm\sqrt{\omega_r\sigma_j/(\mathcal{K}_y k_m)}$. We can see that the position of the maximum of the diffusivity for the fast ions is dependent only on the phase velocity of the background mode and on the magnetic geometry through the $\mathcal{K}_y$ term. With the known expression for $\mathcal{K}_y$ in $\hat{s}$-α geometry, we have

$$v_{\parallel,0}^2 = -\frac{R}{2L_\perp}\frac{\omega_r\sigma_j}{k_m[\cos(z)+\hat{s}z\sin(z)]}. \quad (18)$$

These root lines in the $v_\parallel$-z plane are depicted in Fig. 5 for different background gradients. All show a similar behavior, with a broad area for low velocities, where they extend from $z=-2$ to $z=2$. Then the roots quickly go to higher $v_\parallel$ values. This happens because the geometrical factor $\mathcal{K}_y$ approaches zero at $z_0=2.7093$. Despite these roots for high parallel velocities, we do not find any high $v_\parallel$ contributions to the fast particle flux. The reason is that there are only two regions in the parallel z direction which contribute to the particle flux (near $z=\pm z_0$) and they become narrower. Hence, integrated over the parallel coordinate, the total particle flux goes down with $v_\parallel$. This argument can also be used to quantitatively explain the $v_\parallel^{-2}$ decay observed for high velocities (cf. Figs. 9 and 11 below). To match the real frequency, the parallel position must approach z_0 if $v_\parallel$ increases. So for high enough velocities, $\mathcal{K}_y$ can be Taylor expanded around z_0 which gives $c_0(z-z_0)$. That linear approximation is good enough can be seen in Fig. 10 below. Putting this approximation into the Doppler shifted frequency of the prefactor of Eq. (17), we can write this prefactor as

$$\frac{(\gamma/C_v)^2}{(\omega_r/C_v+z_0-z)^2+(\gamma/C_v)^2}$$

with $C_v=v_\parallel^2 k_m c_0/\sigma_j$. This is a Lorentz shaped function in the variable z with a width of γ/C_v. This width is proportional to $v_\parallel^{-2}$ as can be clearly seen. As the integral over z for higher velocities is proportional to the width of the Lorentz shaped functions near z_0, the total flux contribution shows the same $v_\parallel$ dependency.

Additionally in an intermediate range of $v_\parallel$, where the peaks of the prefactor approach $\pm z_0$, the ballooning structure of the background electrostatic potential also reduces the flux. Due to this structure, the weighting of contributions from the high field side is much weaker than from the low field side (z around zero).

Physically, the condition expressed by Eq. (18) means that for particles with that particular velocity, the toroidal drift velocity is in resonance with the diamagnetic drift velocity of the turbulence. Sufficiently close to this resonance point, the fast particle diffusivity is expected to be comparable to the diffusivities characterizing the background tur-

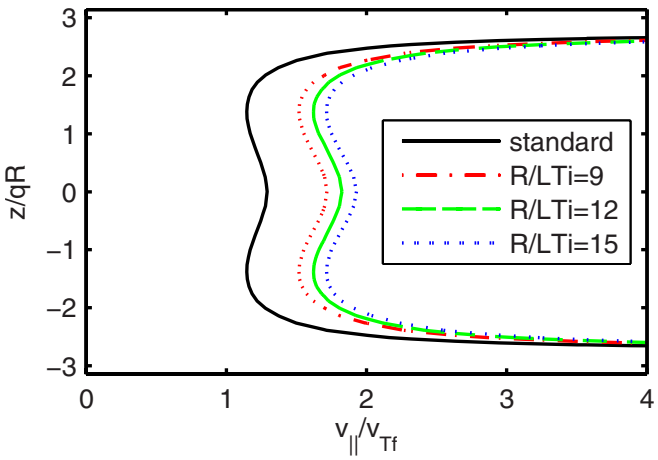

FIG. 5. (Color online) Curves in the $v_\parallel$-z plane where the Doppler shifted frequency ω' vanishes for the standard case (black, solid line), and for a R/L_{Ti} scan with $R/L_n=R/L_{Te}=0$. The values for the ion temperature gradient are 9 (red, dashed line), 12 (green, dashed-dotted line), and 15 (blue, dotted line).

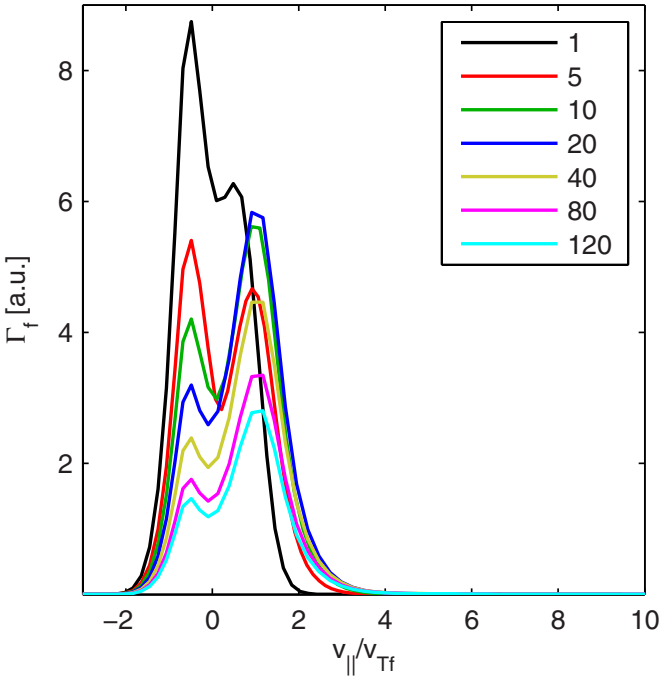

FIG. 6. (Color online) Fast particle transport Γ_f as a function of the parallel velocity $v_{\|}$ for $\tau_+=1$ (black line), $\tau_+=5$ (red line), $\tau_+=10$ (green line), $\tau_+=20$ (blue line), $\tau_+=40$ (yellow line), $\tau_+=80$ (magenta line), and $\tau_+=120$ (cyan line).

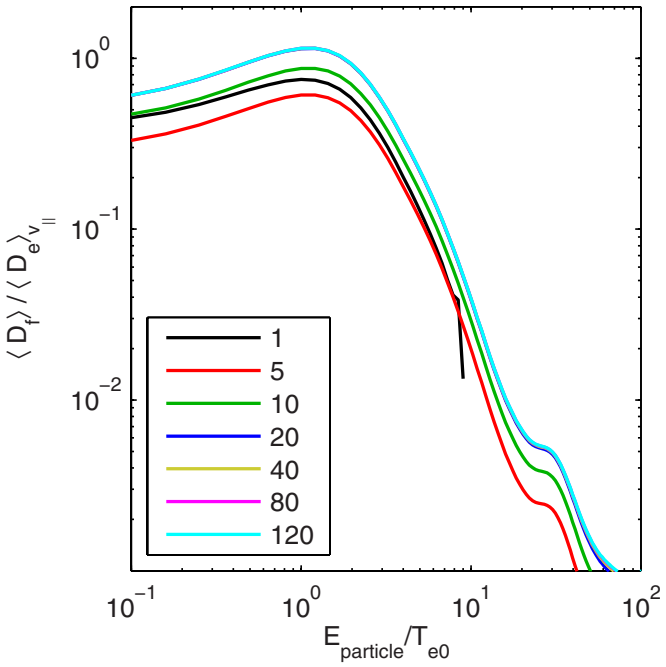

FIG. 7. (Color online) Fast particle diffusivity $\langle D_f \rangle$ as a function of the parallel velocity $v_{\|}$ for $\tau_+=1$ (black line), $\tau_+=5$ (red line), $\tau_+=10$ (green line), $\tau_+=20$ (blue line), $\tau_+=40$ (yellow line), $\tau_+=80$ (magenta line), and $\tau_+=120$ (cyan line). The curves that are not visible lie under the cyan ($\tau_+=120$) curve.

bulence. We note in passing that nonlinearly, the growth rate γ is to be replaced by the inverse of the turbulence correlation time τ_c, and the phase velocity ω/k by the group velocity $\partial\omega/\partial k$ (which, for tokamak core parameters, is often close to the phase velocity in the low-k region of the spectrum, however).

These considerations conclude our discussion of the simplified model. We now turn to the results of linear GENE simulations including all elements of the dynamics. These studies will show that—although a few modifications do occur—the basic intuition obtained within the framework of the above model also applies to fully gyrokinetic situations.

B. Influence of fast ion properties

1. Beam energy

We have seen in Sec. III A that the velocity-dependent fast particle diffusivity is independent of the beam parameter τ_+ (above a threshold in τ_+) for the reduced model. Using the same parameter set as in the last subsection, we now investigate the dependence of the particle flux on the beam energy by means of linear GENE simulations. Some results are shown in Fig. 6. All of these curves only differ in terms of the height of the peaks, but none of them extend to higher velocities. Via the simplified model presented in Sec. III A, we found that the flux divided by the equilibrium distribution does not depend any more on the beam parameter τ_+. This finding can be reproduced here as is shown in Fig. 7 which contains the same data as Fig. 6, but now divided by $F_0(v_{\|})$ and the density gradient. This $v_{\|}$-dependent diffusivity is averaged over the simulation volume and summed over all k_y; the resulting quantity is denoted by $\langle D_f \rangle$ and normalized to $\langle D_e \rangle_{v_{\|}}$ which is calculated as the electron particle flux averaged over the entire simulation volume, summed over all k_y, and divided by the electron density gradient. The result is a measure of how strong the redistribution of fast ions for different particle energies is compared to the diffusivity of the background particles. All curves are very similar and mostly lie on top of each other. Curves for lower values of τ_+ are expected to deviate from the generic high-τ_+ curve, since the reduced model becomes invalid in this regime, and further terms become important in the fast ion Vlasov equation.

These findings confirm our earlier results obtained with the simplified model. As a consequence, instead of looking at different beam energy parameters τ_+, we can choose only one (for example, $\tau_+=40$) and view this case as representative. The redistribution of fast ions for different particle energies for our base case parameters is thus described by Fig. 7. There, the highest fast particle diffusivity occurs for values of the particle energy (defined as $E_{\text{particle}}=v_{\|}^2$ in normalized units) of about $(1-2)E_{\text{thermal}}$. For higher velocities, one finds a power-law decrease to very low values, and for energies above $10E_{\text{thermal}}$, there occur some resonances, but their contribution to the total fast ion diffusivity is negligible. As we will discuss below, the resonance energy can be larger than the one found for the nominal case (actually as large as about $10E_{\text{thermal}}$), but very importantly, the velocity range for which the fast ions are redistributed by the background microinstabilities is independent of the beam energy. Instead, it is set by the thermal energy of the background plasma.

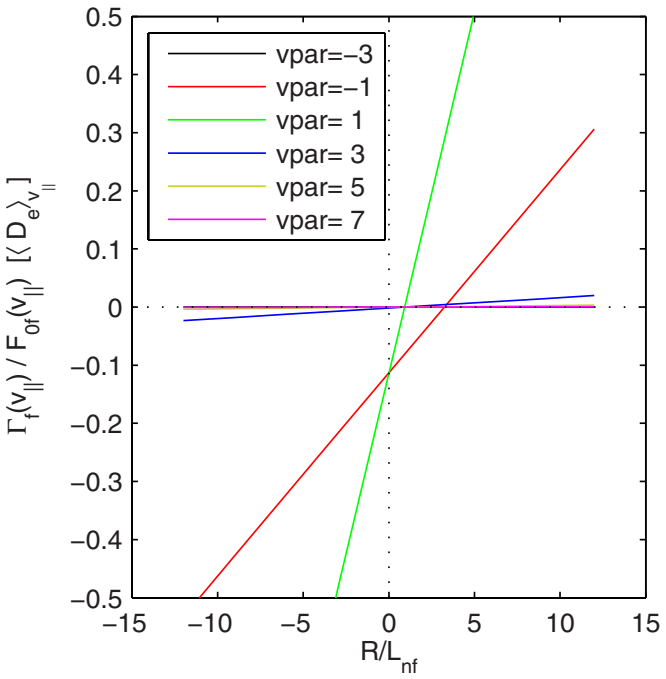

FIG. 8. (Color online) Fast particle flux Γ_f as a function of the fast ion density gradient for $\tau_+=40$. The different lines indicate different parallel velocities of the fast particles.

2. Fast ion density gradient

The second important parameter characterizing the fast ion species (besides the beam energy which is given by the parameters $\tau_\pm$) is the density gradient of the fast ions. Our simple model, Eq. (13), suggests a linear dependence of the particle flux on the density gradient. It also implies that for vanishing gradients the flux also vanishes. But the model has been constructed to describe cases with strong (and experimentally relevant) gradients like $R/L_n=15$, so it is not clear if it will also hold for much smaller gradients. In Fig. 8, the particle flux from linear simulations are shown as a function of the density gradient for different particle energies. The dependency is clearly linear, so it is appropriate to calculate the diffusivities as slopes of the lines. It can also be seen that all lines show a small inward transport even if there is no gradient. This inward pinch varies with the particle energy. As we cannot explain this negative flux by means of our simple model, the origin of this pinch effect must be connected to some of the terms that have been neglected, namely, the parallel dynamics or the curvature term for the electrostatic potential. Since we need a coupling of the fast ion Vlasov equation to the fields of the background microinstabilities, and since for low density gradients, the drive term cannot play that role, we have to take into account also the other field coupling terms to explain the pinch effect of the fast ions.

Reducing again the fast ion Vlasov equation, and observing carefully the change of the pinch, we can attribute the inward transport to the term

$$\left[\frac{F_0\mu\hat{B}}{2\tau_\perp}+v_\parallel^2\left(\frac{F_{0-}}{\tau_-}+\frac{F_{0+}}{\tau_+}\right)\right]\left(\mathcal{K}_x\frac{\partial\chi}{\partial x}+\mathcal{K}_y\frac{\partial\chi}{\partial y}\right) \tag{19}$$

in the Vlasov equation. Now, as we know, that this term is responsible for the pinch, we extend our simplified model for the fast ions Vlasov equation by combining Eqs. (13) and (19) to

$$\frac{\partial F_1}{\partial t}+\omega_{n_j}F_0\frac{1}{\hat{B}}\frac{\partial\bar{\Phi}_1}{\partial y}+\frac{v_\parallel^2}{\sigma_j}\left(\mathcal{K}_x\frac{\partial F_1}{\partial x}+\mathcal{K}_y\frac{\partial F_1}{\partial y}\right)+v_\parallel^2\left(\frac{F_{0-}}{\tau_-}+\frac{F_{0+}}{\tau_+}\right)\left(\mathcal{K}_x\frac{\partial\bar{\Phi}_1}{\partial x}+\mathcal{K}_y\frac{\partial\bar{\Phi}_1}{\partial y}\right)=0. \tag{20}$$

This yields a generalized response function in (k_x,k_y) Fourier space,

$$F_{n,m}=\frac{\omega_{n_j}F_0\frac{1}{\hat{B}}k_m+v_\parallel^2\left(\frac{F_{0-}}{\tau_-}+\frac{F_{0+}}{\tau_+}\right)(\mathcal{K}_xk_n+\mathcal{K}_yk_m)}{\omega_r-\frac{v_\parallel^2}{\sigma_j}(\mathcal{K}_xk_n+\mathcal{K}_yk_m)+i\gamma}\bar{\Phi}_{n,m}.$$

The particle flux for one k_y mode is now given as the sum over all k_x contributions to the particle flux $\Gamma_m=\Sigma_n\Gamma_{n,m}$. To make these expressions more accessible, we set $k_n=0$ and as we are interested in the pinch effect, we also set $\omega_{n_j}=0$. Thus we get

$$\Gamma_{0,m}=\frac{2k_m^2\pi^{-1/2}\gamma\mathcal{K}_y}{(\sqrt{\tau_-}+\sqrt{\tau_+})\hat{B}}|\Phi_{n,m}|^2\times\left[\frac{1}{\tau_-}\int_{-\infty}^{0}\frac{v_\parallel^2e^{-v_\parallel^2/\tau_-}}{\omega'^2+\gamma^2}dv_\parallel+\frac{1}{\tau_+}\int_0^{\infty}\frac{v_\parallel^2e^{-v_\parallel^2/\tau_+}}{\omega'^2+\gamma^2}dv_\parallel\right] \tag{21}$$

with the Doppler shifted frequency $\omega'=\omega_r-v_\parallel^2\mathcal{K}_yk_m/\sigma_j$. Both integrals are positive definite, so that the overall sign of the particle flux is given by the prefactor. But here, all quantities are also positive, except for $\mathcal{K}_y$, which changes sign along the field line following coordinate z. For our standard parameters, $\mathcal{K}_y$ is negative on the low-field side where the potential fluctuations are the largest, and this leads to the observed inward flux.

C. Dependence on plasma conditions and magnetic geometry

1. Background density and temperature gradients

In Eq. (17), we found a relation for the diffusivity of the fast ions in terms of the background diffusivity. The prefactor (first term on the right-hand side) is dependent on the real frequencies and growth rates of the microinstabilities driving the background turbulence. These two quantities depend, in turn, on the plasma parameters, and in particular on the density and temperature gradients. In the present section, we will calculate these complex frequencies for variations of plasma parameters about the standard case, and use these values to calculate the prefactor in Eq. (17). In all of the figures in this section, $\langle P\rangle_{z,k_y}$ stands for the prefactor, averaged over the parallel coordinate z and k_y.

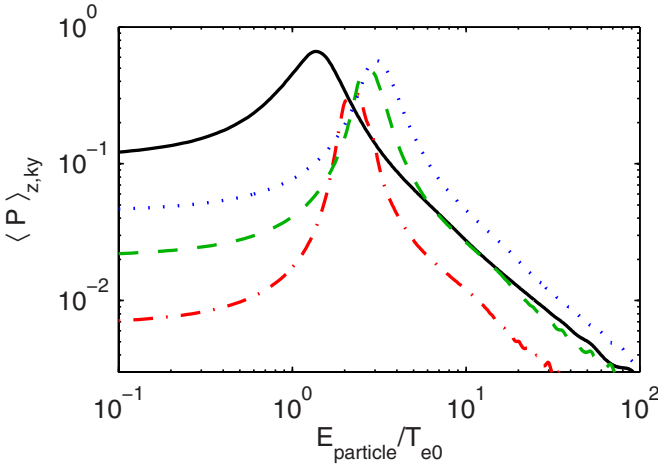

FIG. 9. (Color online) Prefactor in Eq. (17) for $R/L_n=R/L_{Te}=0$ and $R/L_{Ti}=9$ (red, dashed-dotted line), 12 (green, dashed line), and 15 (blue, dotted line). For comparison, the standard case is also shown (black, solid line).

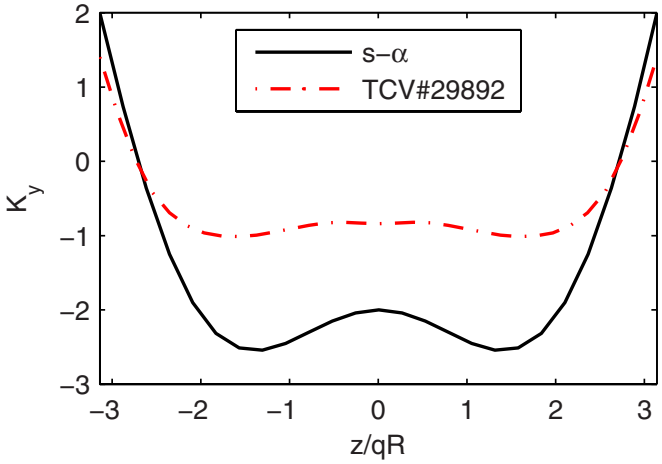

FIG. 10. (Color online) Geometric factor $\mathcal{K}_y$ used for calculating the prefactor in Eq. (17) for real geometry (red, dashed-dotted line) and $\hat{s}$-α geometry (black, solid line).

Let us first consider variations of the ion temperature gradient which acts as a drive for the ITG mode. In Fig. 9, a scan over this parameter is shown. Here, we have chosen the standard parameter set together with a vanishing density and electron temperature gradient. As it turns out, under these "pure" ITG conditions, one obtains larger phase velocities and therefore a shift of the peak of the fast ion diffusivity to higher particle energies. For comparison, the prefactor in Eq. (17) for the nominal parameters is also shown (black solid line).

In Fig. 5, the curves in the $v_\parallel$-z plane are shown for which the Doppler shifted frequency ω' vanishes. This is also where the prefactor of Eq. (17) becomes maximal. For the calculation of the fast ion diffusivity, one must take into account that the background diffusivity usually has a ballooning structure, i.e., it peaks strongly on the low field side (LFS) at $z=0$ and decreases towards the high field side at $z=\pm\pi$. Consequently, the fast particle diffusivity has its $v_\parallel$ peak where the curve in Fig. 5 is in the LFS region. More linear gyrokinetic simulations in $\hat{s}$-α geometry for toroidal ITG modes have shown that the resonance point in $v_\parallel$ space tends to lie in the region $v_\parallel \approx (1-3)v_{Tf}$. However, it should be pointed out in this context that a factor of $\sqrt{2}$ is contained in the definition of $v_{Tf}=\sqrt{2T_{0f}/m_f}$. Moreover, the upper limit may be larger when one considers more realistic tokamak geometries, which is done in the next subsection.

2. Magnetic geometry

According to Eq. (17), the prefactor which connects the fast particle diffusivity to the background diffusivity also depends on the geometrical factor $\mathcal{K}_y$. In $\hat{s}$-α geometry, i.e., for a large aspect ratio, circular cross section tokamak, this factor is simply given by the analytical expression $-2(L_\perp/R)(\cos z+\hat{s}z\sin z)$. We now want to investigate the changes if a more realistic geometry is used. Taking an equilibrium describing the discharge 29892 at 1.0 s in the Tokamak à Configuration Variable (TCV),[35] which has been calculated by means of the CHEASE code,[36] we have performed linear gyrokinetic simulations with GENE. The corresponding geometric factor $\mathcal{K}_y$ is depicted in Fig. 10. This result, in combination with Eq. (17), leads to the curves shown in Fig. 11. It must be mentioned that for this equilibrium we have for the pressure gradient the value of $\partial\beta/\partial x=8\pi p/B_{\mathrm{ref}}p'/p \approx 0.01\cdot 20=0.2$. Therefore it is still valid to use a low-β approximation for the curvature drift.

The difference between the two geometries is striking. The real geometry leads to clearly higher values for the diffusivity for all particle energies than the simplified $\hat{s}$-α geometry. From Fig. 10, we can deduce that $\mathcal{K}_y$ for real geometry is much smaller and therefore would lead to peaks at higher particle energies, if the real frequency were unchanged. However, for the plasma parameters used here, one finds instead that the real frequencies go down by nearly a factor of 3, whereas the growth rates increase strongly. These higher growth rates lead to a much broader Lorentz function for the prefactor which explains the smoother curve in Fig. 11. The peak of the curve is also much less pronounced and

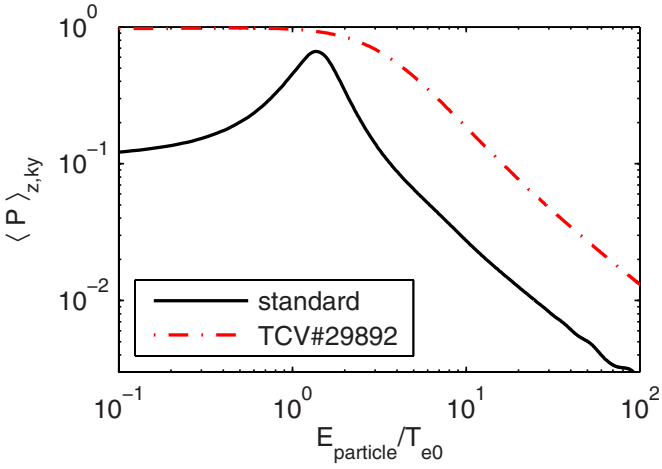

FIG. 11. (Color online) Prefactor in Eq. (17) for real geometry (red, dashed-dotted line) and $\hat{s}$-α geometry (black, solid line) with the same gradients.

shifted to lower particle energies. For low energies, the growth rate dominates the Doppler shifted frequency and therefore leads to a value close to unity.

A general insight gained in the present section is that general geometry is able to affect both the toroidal drift velocities of the fast ions as well as the diamagnetic drift of the background turbulence, and thus the energy-dependent fast ion diffusivity. Under regular tokamak core conditions, one may expect a significant radial redistribution of energetic particles only in the low-energy region of the slowing-down distribution, up to about ten times the thermal energy of the background plasma. In the next section, this view, which has been developed on the basis of linear considerations, shall be tested in the context of nonlinear simulations.

IV. NONLINEAR SIMULATIONS

In the following, we will show the results of turbulence simulations, adopting the following approach. We will first perform a nonlinear GENE simulation with only two species (electrons and main ions), and run it up to a point where the turbulence is clearly saturated. Then we introduce the fast ions as a third passive species using the Vlasov equation (5) with the asymmetric Maxwell equilibrium distribution mentioned above. This third species is introduced with zero amplitude, so a short transient phase follows the start until the fast particles find to a dynamic equilibrium with the imposed turbulent fields.

The physical parameters are the same as indicated in Sec. III. The radial box size was $100\rho_s$, the minimal $k_y\rho_s$ was chosen to be 0.05. We used 96 grid points in radial direction and employed 16 modes in the binormal direction. Along the field line, 16 points were used. In velocity space, the μ direction was resolved with 8 points chosen as Gaussian integration knots in a range from 0 to 9 in normalized units. $v_\parallel$ space had 32 equidistant symmetric grid points for the electrons and main ions and 64 points for the beam ions. According to the remarks of Sec. II E, the grid points has been distributed asymmetrically, with 16 for negative $v_\parallel$, and 48 for positive, to have similar resolutions for both directions.

The time trace of the particle flux is shown in Fig. 12. The time average for background and beam ion diffusivity has been calculated from 110 to the end.

A. Particle energy dependence of the transport

For the linear runs, we found that the fluxes are dominated by the thermal part of the velocity space, even for the highest beam energies. Here, we will test if this characteristic property also holds in nonlinear situations. In Fig. 13, the particle diffusivity is shown as a function of the particle energy. It is clear from this figure that the overall behavior is very similar to the one observed in linear simulations. Again, there is a contribution to the fast particle diffusivity at low and intermediate particle energies. But one interesting difference can also be observed: The slope of the decrease in this double logarithmic plot changes. Up to $E_{\text{particle}} \approx 10T_{e0}$, the diffusivity decreases stronger with the particle energy than for energies above this threshold. In the latter regime, the decrease is slower, exhibiting a E^{-1}_{particle} falloff.

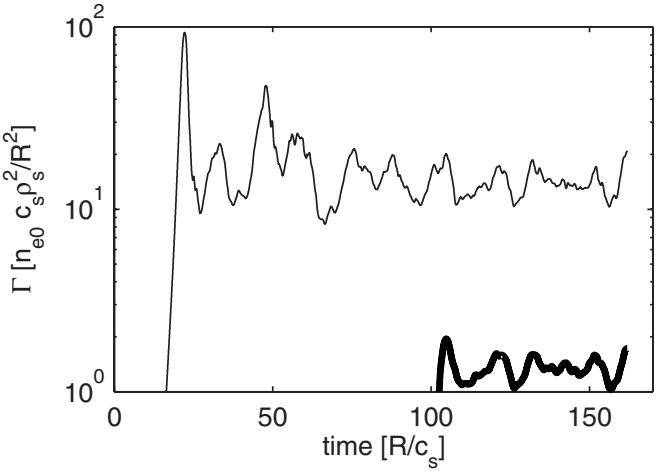

FIG. 12. Time trace of the particle flux of the electrons (thin line) and the $\tau_+=40$ fast ions (thick line) for a nonlinear simulation.

It can also be seen from a simulation in which the term in the full fast particle Vlasov equation, which describes the $E\times B$ advection of the perturbed distribution function [the fifth term in Eq. (5)], has been switched off, that this term is not responsible for the different slopes in the decrease of the diffusivity. Neither do the different k_y components exhibit different dependencies on the particle energy. So the origin of this deviation from the linear behavior must lie in the spatiotemporal structure of the turbulent background fields.

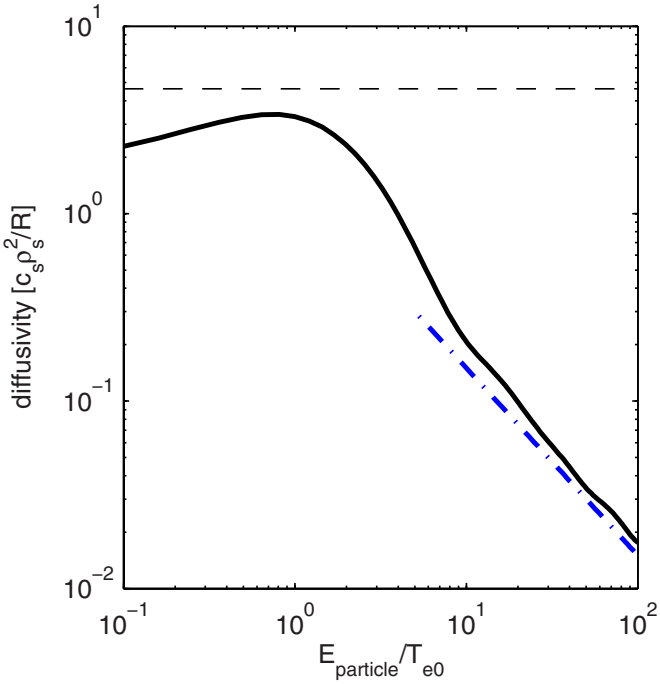

FIG. 13. (Color online) Fast particle diffusivity as a function of particle energy with a turbulent background. The dashed-dotted (blue) curve indicates a $(E_{\text{particle}}/T_{0e})^{-1}$ decrease. The particle diffusivity of the background turbulence is $D_{\text{turb}}=4.6c_s\rho_s^2/R$.

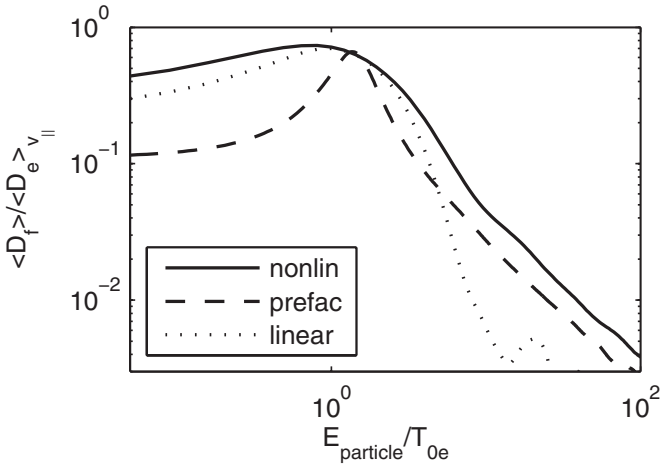

FIG. 14. Comparison of the nonlinear (solid line) to the simplified (dashed line) and the full linear (dotted line) model. Shown is the ratio of beam ion diffusivity (averaged over all k_y and z) to the background diffusivity.

B. Comparison of the models

Up to now, we used three different methods to determine the dependency of the beam ion diffusivity on the particle energy. First, we employed linear simulations; second, we constructed a simplified quasilinear model; and third, we performed fully nonlinear simulations to find the beam ion particle flux. In Fig. 14, we compare these three models. All three curves show a peak at $E_{\text{particle}} \sim T_{0e}$. For lower energies the simplified model deviates from the other curves, but this is clear, since we constructed the model with respect to the higher energies. It is not any more appropriate to neglect the other terms in the Vlasov equation for lower energies.

The next point is that all models show a clear decrease for higher energies. But the slopes are different. It is astonishing that the simplified model better reproduces the E_{particle}^{-1} decay of the nonlinear simulations than the linear model does.

C. Density gradient dependence

In the linear investigations shown in Sec. III B 2, we found a linear dependence of the fast ion particle flux on the fast ion density gradient. In addition, we saw a small pinch effect. These findings also carry over to the fast ion heat fluxes. To test if these properties still hold in nonlinear situations, we carry out a density gradient scan employing the values $R/L_n = 15, 3, 0, -3, -12$. The results are shown in Fig. 15. Indeed, we find again a linear dependence with a small particle and heat pinch. From these simulations, we can calculate the diffusivity of the fast ions and get $D_f = 5.0 c_s \rho_s^2/R$. Compared to the diffusivity of the background turbulence, where we find $D_{\text{turb}} = 4.6 c_s \rho_s^2/R$, the fast particle diffusivity is comparable to the background diffusivity. The differences to the previous subsection, where one can find a smaller diffusivity for the beam ions, are due to a different averaging time window. The simulations in the present subsection are computationally demanding and therefore only a short time trace has been followed. For the qualitative conclusion of a linear dependence of the beam ion particle flux on the beam ion density gradient, this is enough. For better quantitative comparisons, the simulations have to be longer. More nonlinear simulation results will be reported in a subsequent publication.

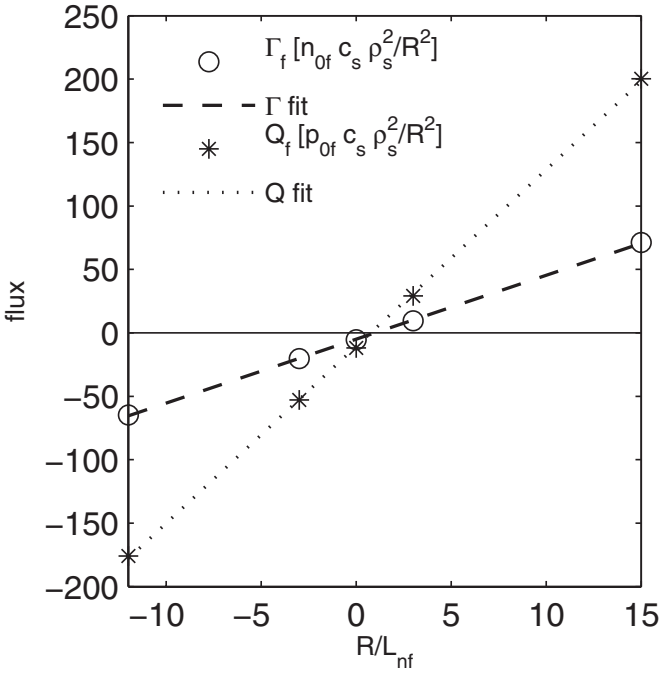

FIG. 15. Density gradient scan for the particle flux (○, dashed line) and for the heat flux (*, dotted line) in nonlinear simulations. The lines are linear fits to the data.

V. SUMMARY AND CONCLUSIONS

In the present paper, we investigated the transport of fast beam ions by background turbulence via linear and nonlinear gyrokinetic simulations with the GENE code. For this purpose, the usual gyrokinetic equations found in the literature were generalized to a situation in which one of the particle species (describing the fast ions) is characterized by an asymmetric and anisotropic Maxwellian equilibrium distribution. Using two main species to produce the background turbulence, we introduced the fast ions as tracer particles into these background fields and measured the fast ion diffusivity as a function of the particle energy (or parallel velocity).

Using a simplified model as well as linear and nonlinear GENE simulations, we found that the diffusivity of the fast ions may reach values comparable to that of the background turbulence if their energy is such that there is a (near-) resonance between their curvature drift velocity and the diamagnetic drift velocity of the background turbulence. The position of that resonance depends both on the magnetic geometry and on the plasma conditions. In any case, it is independent of the beam energy, and one may expect it to lie at up to about 10 thermal energies. Such particles are thus "superthermal" but only moderately energetic. This kind of transport behavior is in line with experimental results from ASDEX Upgrade. In particular, it may serve as an explanation for the observed inefficiency of NBI-induced current drive under certain conditions.[2]

ACKNOWLEDGMENTS

This work was supported in part by the Swiss National Science Foundation.

[1]O. Gruber, H. S. Bosch, S. Gunter, A. Herrmann, A. Kallenbach, M. Kaufmann, K. Krieger, K. Lackner, V. Mertens, R. Neu, F. Ryter, J. Schweinzer, A. Stabler, W. Suttrop, R. Wolf, K. Asmussen, A. Bard, G. Becker, K. Behler, K. Behringer, A. Bergmann, M. Bessenrodt-Weberpals, K. Borrass, B. Braams, M. Brambilla, R. Brandenburg, F. Braun, H. Brinkschulte, R. Bruckner, B. Brusehaber, K. Buchl, A. Buhler, H. P. Callaghan, A. Carlson, D. P. Coster, L. Cupido, S. D. Hempel, C. Dorn, R. Drube, R. Dux, S. Egorov, W. Engelhardt, H. U. Fahrbach, U. Fantz, H. U. Feist, P. Franzen, J. C. Fuchs, G. Fussmann, J. Gafert, G. Gantenbein, O. Gehre, A. Geier, J. Gernhardt, E. Gubanka, A. Gude, G. Haas, K. Hallatschek, D. Hartmann, B. Heinemann, G. Herppich, W. Herrmann, F. Hofmeister, E. Holzhauer, D. Jacobi, M. Kakoulidis, N. Karakatsanis, O. Kardaun, A. Khutoretski, H. Kollotzek, S. Kotter, W. Kraus, B. Kurzan, G. Kyriakakis, P. T. Lang, R. S. Lang, M. Laux, L. L. Lengyel, F. Leuterer, A. Lorenz, H. Maier, M. Manso, M. Maraschek, M. Markoulaki, K. F. Mast, P. J. McCarthy, D. Meisel, H. Meister, R. Merkel, J. P. Meskat, H. W. Muller, M. Munich, H. Murmann, B. Napiontek, G. Neu, J. Neuhauser, M. Niethammer, J. M. Noterdaeme, G. Pautasso, A. G. Peeters, G. Pereverzev, S. Pinches, G. Raupp, K. Reinmuller, R. Riedl, V. Rohde, H. Rohr, J. Roth, H. Salzmann, W. Sandmann, H. B. Schilling, D. Schlogl, E. Schmidtmann, H. Schneider, R. Schneider, W. Schneider, G. Schramm, S. Schweizer, R. R. Schworer, B. D. Scott, U. Seidel, F. Serra, S. Sesnic, C. Sihler, A. Silva, E. Speth, K. H. Steuer, J. Stober, B. Streibl, A. Thoma, W. Treutterer, M. Troppmann, N. Tsois, W. Ullrich, M. Ulrich, P. Varela, H. Verbeek, O. Vollmer, H. Wedler, M. Weinlich, U. Wenzel, F. Wesner, R. Wunderlich, N. Xantopoulos, Q. Yu, D. Zasche, T. Zehetbauer, H. P. Zehrfeld, H. Zohm, and M. Zouhar, Nucl. Fusion **3**, 1321 (1999).

[2]S. Günter, G. Conway, S. daGraça, H.-U. Fahrbach, C. Forest, M. Garcia Munoz, T. Hauff, J. Hobirk, V. Igochine, F. Jenko, K. Lackner, P. Lauber, P. McCarthy, M. Maraschek, P. Martin, E. Poli, K. Sassenberg, E. Strumberger, G. Tardini, E. Wolfrum, H. Zohm, and ASDEX Upgrade Team, Nucl. Fusion **47**, 920 (2007).

[3]M. C. Zarnstorff, G. Bateman, S. H. Batha, M. Beer, M. G. Bell, R. E. Bell, H. Biglari, M. Bitter, R. Boivin, N. L. Bretz, R. V. Budny, C. E. Bush, J. D. Callen, Z. Chang, L. Chen, C. Z. Cheng, S. C. Cowley, D. S. Darrow, R. D. Durst, P. C. Efthimion, R. J. Fonck, E. D. Fredrickson, G. Y. Fu, H. P. Furth, G. J. Greene, B. Grek, L. R. Grisham, G. W. Hammett, R. J. Hawryluk, W. W. Heidbrink, K. W. Hill, S. P. Hirshman, D. J. Hoffman, J. C. Hosea, M. Hughes, R. A. Hulse, A. C. Janos, D. L. Jassby, F. C. Jobes, D. W. Johnson, L. C. Johnson, J. Kamperschroer, J. Kesner, H. Kugel, P. H. LaMarche, B. LeBlanc, F. Levinton, J. S. Machuzak, R. Majeski, D. M. Manos, D. K. Mansfield, E. S. Marmar, M. E. Mauel, E. Mazzucato, M. P. McCarthy, D. C. McCune, K. M. McGuire, D. M. Meade, S. S. Medley, D. R. Mikkelsen, D. A. Monticello, D. Mueller, M. Murakami, J. Murphy, Y. Nagayama, G. A. Navratil, R. Nazikian, D. K. Owens, H. K. Park, W. Park, S. F. Paul, F. W. Perkins, E. Perry, C. K. Phillips, M. Phillips, S. Pitcher, N. Pomphrey, D. A. Rasmussen, M. H. Redi, G. Rewoldt, F. Rimini, D. Roberts, A. L. Roquemore, S. A. Sabbagh, G. Schilling, J. Schivell, G. L. Schmidt, S. D. Scott, J. A. Snipes, J. E. Stevens, W. Stodiek, J. D. Strachan, B. C. Stratton, E. J. Synakowski, W. M. Tang, G. Taylor, J. L. Terry, M. Thompson, H. H. Towner, H. Tsui, M. Tuszewski, M. Ulrickson, S. Von Goeler, A. Von Halle, R. M. Wieland, M. Williams, J. R. Wilson, K. L. Wong, P. Woskov, G. A. Wurden, M. Yamada, K. M. Young, and S. J. Zweben, in *Proceedings of the 14th International Conference on Plasma Physics and Controlled Nuclear Fusion Research* (International Atomic Energy Agency, Vienna, 1993), Vol. 1, p. 111.

[4]P. C. Efthimion, M. Bitter, E. D. Fredrickson, R. J. Goldston, G. W. Hammett, K. W. Hill, H. Hsuan, R. A. Hulse, R. Kaita, D. K. Mansfield, D. C. McCune, K. M. McGuire, S. S. Medley, D. Mueller, A. T. Ramsey, S. D. Scott, B. C. Stratton, K.-L. Wong, TFTR Group, H. Biglari, P. H. Diamond, Y. Takase, and V. A. Vershkov, in *Proceedings of the 12th International Conference on Plasma Physics and Controlled Nuclear Fusion Research* (International Atomic Energy Agency, Vienna, 1989), Vol. 1, pp. 307–321.

[5]S. J. Zweben, R. L. Boivin, M. Diesso, S. Hayes, H. W. Hendel, H. Park, and J. D. Strachan, Nucl. Fusion **30**, 1551 (1990).

[6]W. W. Heidbrink, C. W. Barnes, G. W. Hammett, Y. Kusama, S. D. Scott, M. C. Zarnstorff, L. C. Johnson, D. McCune, S. S. Medley, H. K. Park, A. L. Roquemore, J. D. Strachan, and G. Taylor, Phys. Fluids B **3**, 3167 (1991).

[7]S. J. Zweben, R. L. Boivin, C.-S. Chang, G. W. Hammett, and H. E. Mynick, Nucl. Fusion **31**, 2219 (1991).

[8]S. J. Zweben, D. S. Darrow, E. D. Fredrickson, and H. E. Mynick, Nucl. Fusion **33**, 705 (1993).

[9]T. Hauff and F. Jenko, Phys. Plasmas **14**, 092301 (2007).

[10]T. Dannert and F. Jenko, Phys. Plasmas **12**, 072309 (2005).

[11]F. Merz and F. Jenko, Phys. Rev. Lett. **100**, 035005 (2008).

[12]M. Vlad, F. Spineanu, J. H. Misguich, and R. Balescu, Phys. Rev. E **58**, 7359 (1998).

[13]V. Naulin, A. H. Nielsen, and J. J. Rasmussen, Phys. Plasmas **6**, 4575 (1999).

[14]S. V. Annibaldi, G. Manfredi, and R. O. Dendy, Phys. Plasmas **9**, 791 (2002).

[15]R. Basu, T. Jessen, V. Naulin, and J. J. Rasmussen, Phys. Plasmas **10**, 2696 (2003).

[16]M. Vlad, F. Spineanu, J. H. Misguich, J. D. Reuss, R. Balescu, K. Itoh, and S. I. Itoh, Plasma Phys. Controlled Fusion **46**, 1051 (2004).

[17]M. Vlad and F. Spineanu, Phys. Rev. E **70**, 056304 (2004).

[18]B. D. Scott, Phys. Plasmas **12**, 082305 (2005).

[19]C. Estrada-Mila, J. Candy, and R. E. Waltz, Phys. Plasmas **12**, 022305 (2005).

[20]G. Manfredi and R. O. Dendy, Phys. Rev. Lett. **76**, 4360 (1996).

[21]G. Manfredi and R. O. Dendy, Phys. Plasmas **4**, 628 (1997).

[22]M. Vlad and F. Spineanu, Plasma Phys. Controlled Fusion **47**, 281 (2005).

[23]M. Vlad, F. Spineanu, S. I. Itoh, M. Yagi, and K. Itoh, Plasma Phys. Controlled Fusion **47**, 1015 (2005).

[24]T. Hauff and F. Jenko, Phys. Plasmas **13**, 102309 (2006).

[25]C. Estrada-Mila, J. Candy, and R. E. Waltz, Phys. Plasmas **13**, 112303 (2006).

[26]F. Jenko, W. Dorland, M. Kotschenreuther, and B. N. Rogers, Phys. Plasmas **7**, 1904 (2000).

[27]E. A. Frieman and L. Chen, Phys. Fluids **25**, 502 (1982).

[28]T. S. Hahm, Phys. Fluids **31**, 2670 (1988).

[29]T. S. Hahm, W. W. Lee, and A. Brizard, Phys. Fluids **31**, 1940 (1988).

[30]A. Brizard, Phys. Fluids B **1**, 1381 (1989).

[31]M. A. Beer, S. C. Cowley, and G. W. Hammett, Phys. Plasmas **2**, 2687 (1995).

[32]P. Xanthopoulos and F. Jenko, Phys. Plasmas **13**, 092301 (2006).

[33]J. W. Connor, R. J. Hastie, and J. B. Taylor, Phys. Rev. Lett. **40**, 396 (1978).

[34]T. Dannert, Ph.D. thesis, Technische Universität München, 2005, http://tumb1.biblio.tu-muenchen.de/publ/diss/ph/2005/dannert.pdf.

[35]F. Hofmann, J. B. Lister, M. Anton, S. Barry, R. Behn, S. Bernel, G. Besson, F. Buhlmann, R. Chavan, M. Corboz, M. J. Dutch, B. P. Duval, D. Fasel, A. Favre, S. Franke, A. Heym, A. Hirt, C. Hollenstein, P. Isoz, B. Joye, X. Llobet, J. C. Magnin, B. Marletaz, P. Marmillod, Y. Martin, J. M. Mayor, J. M. Moret, C. Nieswand, P. J. Paris, A. Perez, Z. A. Pietrzyk, R. A. Pitts, A. Pochelon, R. Rage, O. Sauter, G. Tonetti, M. Q. Tran, F. Troyon, D. J. Ward, and H. Weisen, Plasma Phys. Controlled Fusion **36**, B277 (1994).

[36]H. Lütjens, A. Bondeson, and O. Sauter, Comput. Phys. Commun. **97**, 219 (1996).